Hydrodynamical graphene - where every electron counts

Molecular dynamics study of relativistic charge flow

Piotr Benedysiuk

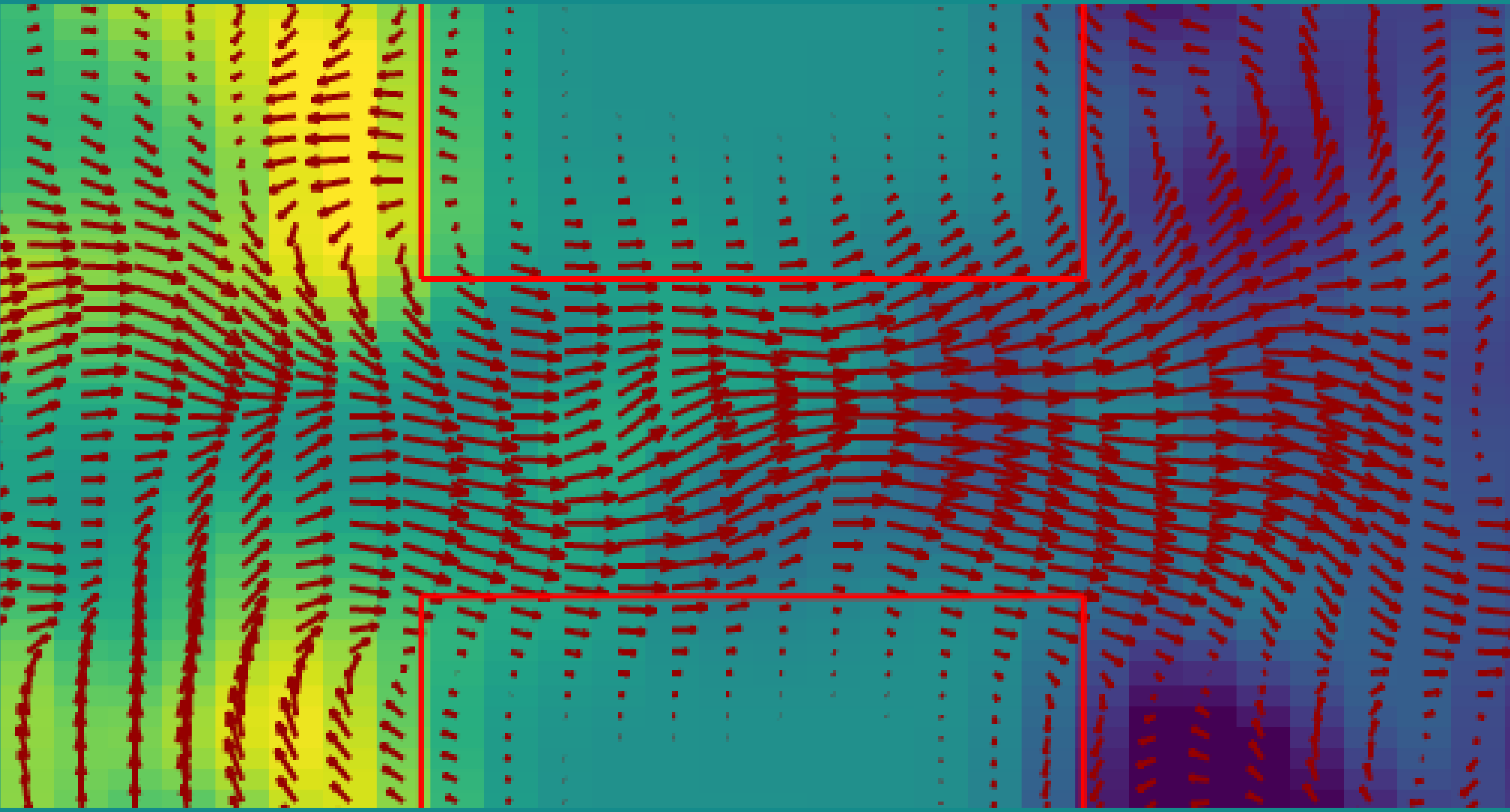

TU Delft

Hydrodynamical graphene - where every electron counts

Molecular dynamics study of relativistic charge flow

by

Piotr Benedysiuk

to obtain the degree of Master of Science
at the Delft University of Technology,
to be defended publicly on Wednesday March 27, 2019 at 15:30 pm.

Student number:	4231546	
Thesis committee:	Anton Akhmerov,	TU Delft, supervisor
	Michael Wimmer,	TU Delft
	Toeno van der Sar,	TU Delft

TU Delft

Preface

> It is at this point that normal language gives up, and goes and has a drink.
>
> *Terry Pratchett, The Color of Magic*

In pop culture the human race is often glorified as "explorers", boldly chasing the horizon. Songwriters, movie-makers, poets - all love to romanticize sailors conquering the vast seas underneath skies full of stars. Our society longs for and despairs about the lack of new frontiers to conquer - all from within the safety of their chairs.

It takes a lot to explore. Boldness, dedication, determination, skill, luck will get your ship out of the port and into the open sea and will help you tackle the storms. But sometimes you will find yourself drifting with no wind in sails, directionless and lost in emptiness. It takes true personal strength to convert the inevitable creeping desperation into fuel and to find the wind again.

I consider the period that I have been working on this project as the hardest in my life so far. The project involved many interlocked numerical, programming and physical problems, rocking the foundations of my ship. I would get boogled down in details to no end and would swarm myself with multiple questions - too many to be answered at once - and then promptly fail to answer them all at the same time. Whenever I'd try to get some perspective I'd see myself amidst doldrums.

Now that I am finally approaching land again I realized that the original credo of the project "Flow charts makes for cool plots. Let's make some." indeed led me to the most rewarding parts - and I wish I hadn't lost sight of this truth throughout the journey. If the reader enjoys the figures at least a fraction of as much as I enjoyed making it - then I can happily consider my struggles to be worth it.

With all of this in mind, I'd like to express words of gratitude to some of the people (in no particular order) that have helped me along the way:

The many office mates that I have seen come and go over time - for great input in each others work, for a sense of camaraderie and for keeping each other sane simply by talking;

Elena for being there for me and trying to keep me motivated throughout all of this;

Anton for somehow being able to see the direction for the ship to take - and for making sure this thesis is about physics;

Joe for having a huge impact on the code - without you, I'd still be trying to figure it out;

Dennis and Jesse for all of the hours spend cracking heads over cards, games and the horrors of my grammar - thank you for reading the raw version of this document!;

And to all great people, I have met here in Delft - thanks to you all I have never doubted starting this random walk known as studying.

Piotr Benedysiuk
Delft, March 2019

Contents

1 Introduction **1**

2 Theory **3**
- 2.1 Dispersion of graphene . . . 3
- 2.2 Coulomb interaction . . . 3
- 2.3 Bulk density and scaling . . . 4
- 2.4 Observables . . . 6

3 Methods **9**
- 3.1 Equations of motion . . . 9
- 3.2 Negative potential domination . . . 10
- 3.3 Boundary conditions . . . 11
- 3.4 Leads . . . 13
- 3.5 Geometries . . . 13
- 3.6 Physical observables as functions of spatial coordinates . . . 14

4 Results **17**
- 4.1 Stability of the numerical approach . . . 17
  - 4.1.1 Fermi regime . . . 17
  - 4.1.2 Dirac regime . . . 18
- 4.2 Viscosity effects . . . 19
- 4.3 I-V characteristics at high bias . . . 19
  - 4.3.1 Typical particle drift velocity . . . 19
  - 4.3.2 Conductance correlation at different bias . . . 20
  - 4.3.3 Viscosity and conductance correlation . . . 20

5 Conclusion **23**

A DoS derivations **25**
- A.1 Structure of graphene . . . 25
  - A.1.1 Lattice structure . . . 25
  - A.1.2 Tight binding model . . . 25
- A.2 Scaling properties . . . 26

B Leapfrog properties and stability **31**
- B.1 Mathematical background of the numerical integration scheme . . . 31
- B.2 Error terms . . . 31
- B.3 Bouncing . . . 32

C Smoothing of local observables **35**
- C.1 Physical observables as functions of spatial coordinates . . . 35

Bibliography **37**

1

Introduction

Graphene is one of the more exotic materials in the field of condensed matter physics. This two-dimensional honeycomb shaped crystal of carbon atoms is a textbook example of a Dirac material. Dirac materials are characterized by linear dispersion relation of the charge carriers and vanishing density of states at the Dirac point [21] [17][9].

Graphene can be fabricated extremely clean [6] and therefore the transport properties of graphene aren't determined by impurities scattering. Around room temperature charge carriers scatter more often with each other than with phonons. Thus the theory describing transport is one of electron-electron and electron-hole interactions, making graphene very useful in trying to understand particle interactions within Dirac materials. Within this regime, the dynamics become similar to very viscous fluids, where flow is subjected to internal friction.

Recently, in 2016, there has been an experimental breakthrough in the field. A device has been made with which it became possible to measure negative local resistance [5] - a signature of electrons flowing backward at the sides of the channel due to viscosity effects. Suddenly, viscous flow of electrons in graphene became more than a prediction.

This discovery started a small frenzy within the theoretical community. One of the attempts to explain the interactions was based on the Navier-Stokes equations [10]. This approach describes the local dynamics of conserved quantities. As the Coloumb interaction can be long ranged it's unclear if a local theory is sufficient.

Another prominent approach is a model using the Boltzmann transport equation [8]. This equation describes particle distribution functions and how they change in time. Being a statistical-physics approach it can be used in thermodynamical limit only - and therefore it's unclear if one can use it if for low particle numbers.

We propose a third theoretical approach to this problem. Molecular dynamics is a numerical method for approximating the time evolution of the N-body problem. It allows us to compute dynamics of each particle in the system - and as such it is not bounded by the locality of the interactions or number of particles as the previous approaches had been.

The goal of my thesis is to show how to model and simulate charge transport in graphene in the hydrodynamic regime. We will show the theoretical model in Chapter 2, followed by implementation of a device in the framework of molecular dynamics in Chapter 3. Both of these considerations will pay off in the Chapter 4 where we show the effects of interactions on charge transport and the emergence of long-range correlations between charge carriers. Concluding remarks can be found in the Chapter 5 where we conclude the findings and discuss adaptability of the software in order to investigate the prospective options in the field.

2

Theory

In the Section 2.1 I will introduce the effective dispersion relation of graphene and we will understand which particles carry charge within the system. The Coulomb interaction term between these particles will be introduced in the Section 2.2 and we shall see why it's important to introduce this interaction. We will then take a step back in Section 2.3 in order to understand how the interactions scales with relation to temperature and chemical bias, resulting in emergence of two distinct interaction regimes. Lastly in Section 2.4 an explanation will be provided of possible signatures of interactions on the current flow. A curious reader is encouraged to look at the Appendix A for more thorough derivations of all the concepts.

2.1. Dispersion of graphene

The effective Hamiltonian of graphene is well known [19]. It is given by $H = \pm\hbar v_F |\mathbf{k}|$ with $\hbar$ the Planck constant and $v_F = 1 \times 10^6\,\mathrm{m\,s^{-1}}$ the astonishingly high Fermi velocity of charge carriers in graphene. The spectrum consists out of two linear bands touching at $E = 0$. For unbiased graphene the Fermi energy - also referred to as Charge Neutrality Point (CNP) - is exactly the touching point of the two bands. Note the lack of a Fermi surface at the CNP, but unlike an insulator, a small temperature is enough to excite charge carriers - holes for the lower band and electrons for the upper. As we are going to look at transport properties we are only concerned with these positive energy excitations and we write:

$$H = \sum_{\mathrm{e,\,h}} \hbar v_F |\mathbf{k}|, \tag{2.1}$$

for the effective Hamiltonian used. If we now calculate the group velocity of this dispersion we find $\frac{\delta E}{\hbar \delta k} = v_F \hat{\mathbf{k}}$ for all values of $\mathbf{k}$, therefore the charge carried by excitations is carried fast in well-defined directions.
Another way to make graphene conducting is by applying a (arbitrary) small chemical potential. Shifting the Fermi energy up or down will give rise to linearly a growing Fermi surface - unlike conventional 2D metals where the density of states will remain constant. Therefore, applying a chemical potential will create more excitations - and not change how those excitations behave.

Lastly we can recognize this spectrum as a special case of Einsteins energy equation:

$$E^2 = m^2c^4 + p^2c^2,$$

for the case $m = 0$. Indeed, careful [21] computations of the effective mass in graphene gives us $m^* = 0$. The connection to relativistic physics will become more apparent when we consider the equations of motion in the chapter 2.

2.2. Coulomb interaction

As stated before, charge carriers in graphene are electrons and holes carrying opposite charges. In most studies [9] the particle-particle interactions are ignored within their models. However in this section I hope to give an intuitive explanation as to why such interactions are relevant. First start by introducing the 3 dimensional Coulomb interaction potential [2]:

$$V_{ij} = \frac{1}{4\pi\epsilon_0}\frac{q_i q_j}{r_{ij}}, \tag{2.2}$$

with ϵ_0 the vacuum permittivity and q the charge. The total Hamiltonian (after re-scaling by $\hbar v_F$) becomes:

$$H = \sum_i |\mathbf{k}| + \sum_{i,j} \alpha \frac{\pm_{ij}}{r_{ij}} \tag{2.3}$$

with $\pm_{ij} = -1$ if i and j differ in charge and 1 otherwise. The dimensionless parameter $\alpha = \frac{e^2}{4\pi\epsilon_0 \hbar v_F}$ is called the coupling constant. It plays the same role as the fine-structure constant in Quantum Field Theory - it characterizes the strength of charge interactions. In fact the two relate to each other as: $\alpha = \frac{c}{v_F}\alpha_{QFT} \approx \frac{300}{137}$.

In order to get intuitive understanding of the role of α let us consider a (semi) one dimensional strip of graphene of length L. Typical momentum will scale as $k \sim \frac{1}{L}$ and typical particle to particle distance l_{pp} will be proportional to L. Comparing typical kinetic and typical potential energy results in:

$$\frac{V}{E_{kin}} \sim \frac{e^2}{4\pi\epsilon_0 L} \cdot \frac{L}{\hbar v_F} = \alpha.$$

Therefore, naive models tell us that potential energy are of the same order as kinetic. We shall look into the details of this scaling in Section 2.3.

Another relevant aspect is the interplay between the 3D potential and the fact that graphene is a 2D material. In general, screening properties of lower-dimensional systems are suppressed (as compared to higher dimensional systems) [14][17]. Furthermore, the linearity of the spectrum in graphene suppresses the screening. In particular the absence of a Fermi surface at the charge neutrality point leaves us with no states to screen with. As the chemical potential increases the size of Fermi surface increases linearly - as opposed to 2D metals where the Fermi surface is constant everywhere. The important aspect for this work is that the charge carriers can't screen other particles fully. Therefore the potential of a charge carrier interacts with many other particles - making excitations a many-body phenomena.

All of the above considerations show that interactions can form correlations between particles. In more common materials such correlations can still be broken by scattering with impurities. In fact, first theoretical predictions on this topic date all the way back to 1963 [3] - but this result has been mostly forgotten due to lack of clean graphene flakes back in the day. Nowadays it's possible to fabricate **extremely** clean graphene where the typical mean free path is in the order of 1 µm [6] giving a bound on impurity density of $1 \times 10^8\,\mathrm{cm}^{-2}$. We will see later that charge carrier density is orders of magnitude bigger than impurity density, making particle - particle collisions the main scattering source.

When we consider our system to be at (near) charge neutrality electron - hole pairs need to be considered. For a pair of electrons the interaction potential pushes them away, lowering (towards zero) the potential energy. For an electron - hole pair the potential energy is lowered (towards negative infinity) but that happens by pulling the pairs in together (and thus increasing the absolute value of the potential!). This concept can be seen in Figure 2.1 B. In such situations the interactions become even more important for the description of the physics.

2.3. Bulk density and scaling

Physical properties of interactive models such as Equation (2.3) are challenging to compute. In particular, as seen in the previous chapter, the perturbation due to the Coulomb potential is too big for the application of perturbation theory. Furthermore, straightforward diagonalization of the Hamiltonian isn't possible due to huge Hilbert space associated with the system. Lastly, typical tools used in statistical physics are constrained to classical (kinetic energy quadratic in momenta) or weakly-interacting (kinetic energy dominating over the potential) systems. Therefore, in order to build some intuition into physical laws governing interactive graphene systems, we start at the noninteractive Hamiltonian Equation (2.1) and compute the number of charge carriers, charge imbalance and kinetic energy distributions of particles. For exact computations see Appendix A.

To set the stage we first introduce the Density of States (DoS), by computing the change in the number of particles N as we change the energy $\epsilon \to \epsilon + \Delta\epsilon$, normalized by an area of A:

$$\mathrm{DoS} := \frac{1}{A}\frac{\partial N}{\partial \epsilon} = \frac{1}{A}\frac{\partial N}{\partial |k|}\frac{\partial |k|}{\partial \epsilon} = \frac{2_s 2_v}{4\pi^2} \times 2\pi|k| \times \frac{1}{v_F \hbar} = \frac{2_s 2_v |E|}{2\pi\,(v_F \hbar)^2}, \tag{2.4}$$

with the factors of 2 being due to spin and valley degeneracy. In order to include temperature T and chemical potential μ effects to the electron (hole) density n_e (n_h), we use the Fermi-Dirac distribution f_D ($1 - f_D$)

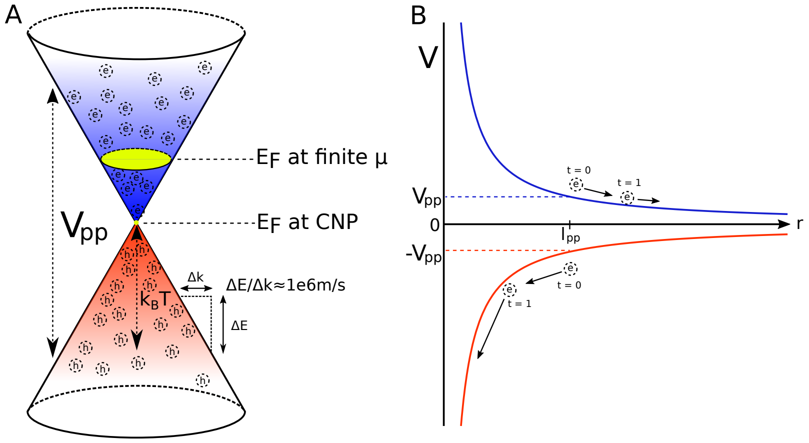

Figure 2.1: A: Graphene's dispersion relation. We show the linear (conic) spectrum and the effects of temperature - exciting charge carriers in each of the two bands. The typical potential between particles is bigger than the energy scale $k_B T$ (see Equation (2.7)) however it is still comparable to the typical kinetic energy. Furthermore, even for low energy excitations this potential is not necessarily the dominant energy scale - interactions with next-nearest particles can change the equations of motions substantially. B: Effects of potential interactions between particles of the same type (top) and opposite type (bottom). The attractive potential between e-h causes the pairs to get closer to each other and the corresponding force between them pulls them in harder as they approach each other. The magnitude of the typical e-h potential will therefore be much higher than V_{pp}.

defined as:

$$f_D := \frac{1}{\exp\left(\beta\left(\epsilon - \mu\right)\right) + 1}, \tag{2.5}$$

with $\beta = (k_B T)^{-1}$ and k_B the Boltzmann constant. Typical effective distribution of states can be seen in figure 2.2

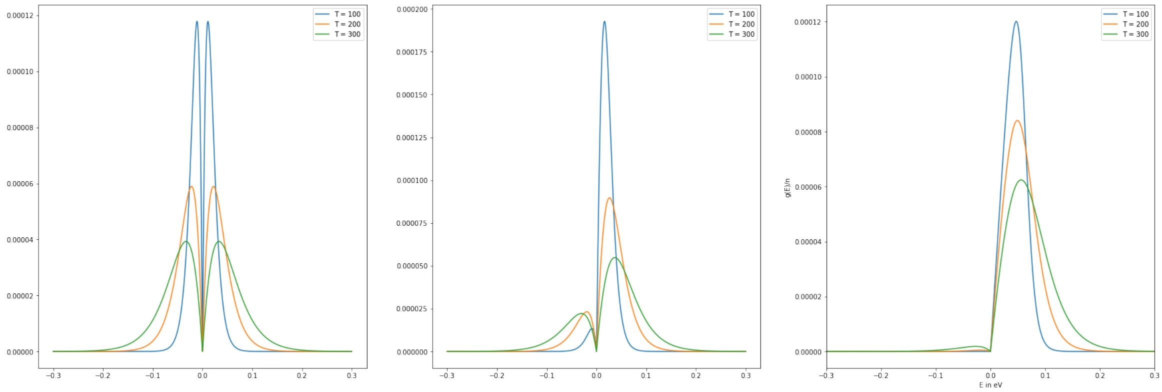

Figure 2.2: Effective DoS for three different cases. First we have the CNP with no chemical potential. The density of holes and electrons is symmetric about zero energy. The second plot is biased with $\mu = 200 k_B$ and we observe the distribution at 100K centering around the chemical potential. Furthermore, most of the excited state are electrons, density of holes is suppressed. Last plot is biased with $\mu = 800 k_B$. Here we see all 3 effective DoS centered around μ. Note that higher temperature ones have bigger spread around μ. Lastly, observe the full suppression of hole excitation.

By straightforwardly integrating the density of states we calculate the total density of charge carriers as the sum of electron and hole contributions.

$$n_e + n_h = \frac{2_s 2_v}{4\pi}\left(\frac{k_B T}{v_F \hbar}\right)^2 \left(\left(\frac{\mu}{k_B T}\right)^2 + \frac{\pi^2}{3}\right). \tag{2.6}$$

To get a feel for the numbers its useful to realize that for $\frac{\mu}{k_B T} < 1$ we can simplify even further and state $n_e + n_h \approx C_{tot} T^2$ with $C_{tot} = 1.43 \times 10^6\,\mathrm{cm}^{-2}\,\mathrm{K}^{-2}$. Therefore, in for T in between 100 and 300 we shall see $\mathcal{O}\left(1 \times 10^{10}\,\mathrm{cm}^{-2}\right)$ charge carriers.

The typical distance between two particles, $l_{pp}^{-1} := \sqrt{n_e + n_h}$, will scale as T^{-1}, thus at higher temperatures the particles will bounce more often. In addition, the typical potential energy between particles will be:

$$V(l_{pp}) \approx \alpha k_B T + \alpha \frac{\mu}{2\pi k_B T}\mu. \tag{2.7}$$

The second term show a very weak dependence on chemical potential. For comparison's sake we compute the typical kinetic energy of this model:

$$E_{kin} \approx 2.2 k_B T + 0.1 \frac{\mu}{2\pi k_B T}\mu. \tag{2.8}$$

Two observations are crucial here. First, the noninteractive model does **not** obey the Equipartition theorem. This is caused by linearity of the spectrum. Therefore we can't assume that potential energy of the interactive model will obey this theorem. In fact, the energy distribution might change significantly due to interactions. Second, at low bias, the ratio of the two energies is roughly 1 - and it moves towards α as μ increases. Note also that changing the temperature does not change the ratio of these two energies - it is only the chemical potential that influences the ratio. However, this does not necessarily mean that interactions are less important at low μ.

In order to understand why interactions remain relevant at low μ, let us consider the charge imbalance of the model. We compute the difference in hole and electron densities:

$$n_h - n_e \approx \frac{2_s 2_v}{2\pi}\left(\frac{k_B T}{v_F \hbar}\right)^2 \left(\log(4)\frac{\mu}{k_B T}\right). \tag{2.9}$$

The scaling is proportional to the product of $k_B T$ and μ. Thus the relative charge imbalance $\frac{n_h - n_e}{n_h + n_e}$ we see that it scales as $\frac{\mu}{k_B T}$. As $\mu \rightarrow 0$ we will see a lower charge imbalance - meaning more interactions will be attractive instead of repulsive. As a result, at low μ, electron and holes will come closer to each other than l_{pp} and therefore they will enhance the typical potential interaction. It is not clear how to compute this effective electron-hole length scale l_{eh}.

It is however clear that this effect depends on the chemical bias and temperature. We can conclude this by considering possible pairs of charge carriers. For l_{eh} to be the most important length scale we need to have many strongly bounded e-h pairs. The number of available charge carriers of both types depends on μ and if we increase it we simply will have less pairs. Therefore at higher μ the effects of negative potential won't be pronounced. This gives rise to different regimes of interactions within graphene - for $\frac{\mu}{k_B T} >> 1$ we obtain a electron/hole Fermi Fluid where potential is an positive quantity and for $\frac{\mu}{k_B T} < 1$ we find a Dirac Fluid where the potential is negative.

2.4. Observables

Interactions between particles leads to the rise of viscous flow within graphene. Most of the literature [7] [8] [10] [5] focuses on the Fermi Fluid regime, however we will remark upon possible observations within the Dirac regime too.

Approximations from hydrodynamical theory [19] in Fermi liquid regime for a narrow rectangular channel gives a conductance of

$$G = \frac{n^2 \omega^3}{12\eta}, \tag{2.10}$$

with ω the width of the channel, n the density of charge carriers and η the viscosity. Within the Fermi regime [19] the resistance (inverse conductance) of a channel should get lowered by temperature - phenomena referred to as the Gurzhi effect [3] - as the viscosity scales roughly as T^{-2}. Analytically this result is a direct cause of the no-slip boundary approximation - velocity vanishes at the boundary.

Another proposal [11] is to observe flow through narrow openings (into bigger spaces) or narrow constrictions (between two bigger spaces). There, again in the Fermi regime, hydrodynamics [19] comes up at:

$$G = \frac{\pi e^2 n^2 \omega^2}{32\eta}, \tag{2.11}$$

which is a very similar result to Eq (2.10) - except for the powers of ω. Remarkably for this analysis the boundary conditions are hard-walls - flow is simply required not to leave the sample. Therefore, the viscosity effects here are a direct manifestation of particle-particle interactions caused by the fluid being funneled into the constraint. The velocity profile in the constriction itself is expected to have a parabolic shape - result known in classical hydrodynamics as Poissele flow. Lastly, near the opening we expect the flow to interact with the funneled flow on the other side. Therefore, there we expect a vortex to appear [11] on outskirts of the main flow through the constriction. Charge carriers in the vortex would move against the current causing (locally) the resistance to be negative. Lastly, constriction geometry is most relevant experimentally - it forces the flow to be dominated by viscosity effects instead other transport mechanism [19] so we will focus on it.

Within the Dirac Fluid regime the charge transfer is more subtle. In particular, it is no longer density of charge carriers and bias voltage that define control the current flow but temperature and energy density. Temperature gradient in particular can cause current flow in graphene which breaks down the Wiedemann-Franz law [19]. We will (briefly) describe how to model temperature gradients within our method in later chapters but it is not the focus of this thesis. However, we will try to simulate current flow by applying a bias (similarly to approach used in Fermi regime) and see if the resulting behaviour of *charge* flow (as opposed to *particle* flow which isn't he same thing in Dirac regime) obeys the Poissele flow shape.

3

Methods

We give a short description of the Molecular Dynamics framework used. We derive the equations of motion (Section 3.1) and discuss most important numerical concerns (Section 3.2). We move on to showing how to model physical necessities for transport such as boundaries (Section 3.3) leads (Section 3.4) and experimental setups where interactions will be visible (Section 3.5). We finish with an innovative approach to computing local values for physical observables (Section 3.6.

3.1. Equations of motion

We model the eigenstates of Hamiltonian (2.3) in the semi-classical approximation, meaning all particles obey the statistical properties given by the dispersion relation but have well defined energies, position and momenta. We also remodel the electron-hole degree of freedom into charge degree of freedom meaning all particles have well-defined charge (positive for holes and negative for electrons). The Hamiltonian locally conserves energy, charge, momentum and angular momentum. Later sections of this chapter will reveal how numerical considerations break these conservation laws.

In our approximation, time-evolution (of the system) is not given by the typical Schrodinger's equation but rather by the Hamilton equations of motion. We already choose to measure energy in $\hbar v_F$, if we now also measure time in terms of v_F and using $\mathbf{p} = \hbar\mathbf{k}$ we can write:

$$\begin{cases} \frac{d\mathbf{k_i}}{dt} & := -\frac{\partial H}{\partial \mathbf{r_i}} = \alpha \sum_j \frac{\pm_{ij}}{|\mathbf{r_{ij}}|^2} \hat{\mathbf{r_{ij}}}, \\ \frac{d\mathbf{r_i}}{dt} & := \frac{\partial H}{\partial \mathbf{k_i}} = \hat{\mathbf{k_i}}. \end{cases} \tag{3.1}$$

The right hand side of Eq (3.1) represents the force (F_i) acting on particle i and the velocity (v_i) respectively. Now the connection to relativistic physics emerges - the velocity of all particles is constant and fully determined by the direction of the wave vector exactly like movement of photons at speed of light. Furthermore, forces acting upon a particle can only change the direction of the particle propagation - never it's speed. In order to compute (time) propagation of the system we approximate the time derivative with discrete time-steps. One should note that the change in momentum is coupled to the positions of all other particles, therefore it's not possible to straightforwardly integrate the PDE (3.1). Furthermore, numerically computing the right hand side of Eq (3.1) involves computing distances between all particles - requiring in the order of $\mathcal{O}(N^2)$ flops. Similarly, computing the values of $\pm_{ij}$ for all particles is also an $\mathcal{O}(N^2)$ operation. All of the other terms are $\mathcal{O}(N)$ operations and thus aren't the main bottleneck for performance. In order for the simulations to be efficient the numerical scheme needs to minimize amount of times force is calculated. Therefore we are looking for an integrator that remains stable even for large time-steps Δt (to minimize the total number of steps) and requires only one calculation of force per time-step.

The integration algorithm is the Leapfrog scheme [12][4]. In this scheme we alternate between updating the velocity and position. Let t_n be the n'th time step and $\mathbf{k_i}$ and $\mathbf{r_i}$ refer to momenta and positions respectively. The update formulae are given by:

$$\begin{cases} \mathbf{k_i}(t_{n+1/2}) & = \mathbf{k_i}(t_n) + F_i(t_n)\frac{\Delta t}{2} \\ \mathbf{r_i}(t_{n+1}) & = \mathbf{r_i}(t_n) + v_i \Delta t \\ \mathbf{k_i}(t_{n+1}) & = \mathbf{k_i}(t_{n+1/2}) + F_i(t_{n+1})\frac{\Delta t}{2}. \end{cases} \tag{3.2}$$

It can be understood as a predictor-corrector approach. We predict the new momentum using the old force, use this new momentum to push positions forward in time and then correct the momentum using the newly computed force. Attentive readers might notice that even though we use the force twice per iteration, the "new" force calculated becomes the "old" force in next iteration. Therefore we only need to compute force once per iteration. Minimal memory footprint of this integration scheme is 6 floats (two each for position, momentum and force) and one integer (charge) per particle. Leapfrog belongs to the class of sympletic algorithms allowing for energy conservation on long timescales. More in depth description of the properties of Leapfrog can be found in the Appendix B.

3.2. Negative potential domination

The inter-particle potential Eq (2.2) diverges as $r_{ij} \to 0$. In case of e-e (or h-h) interaction this divergence isn't relevant as conservation of energy pushes the particles away, preventing them from ever reaching the singularity. However e-h interaction is attractive and thus particles do tend to get closer to each other. In principle conservation of momentum and angular momentum should keep such pairs from collapsing onto each other, but due to discrete time stepping in numerical integration it becomes possible for non-physical solutions to occur. In particular, whenever particles come close the magnitude of forces acting on the particles becomes very large. The issue is that regardless of the momentum the particles move at constant velocity - and thus during the timesteps the numerical error made by updating the positions and the momenta out of sync (instead of continuously) accumulates violating the conservation of energy. This phenomena is called a breakdown of stability - and in case of diverging potential it's notoriously hard to derive any sensible bounds on Δt in order to prevent it [13].

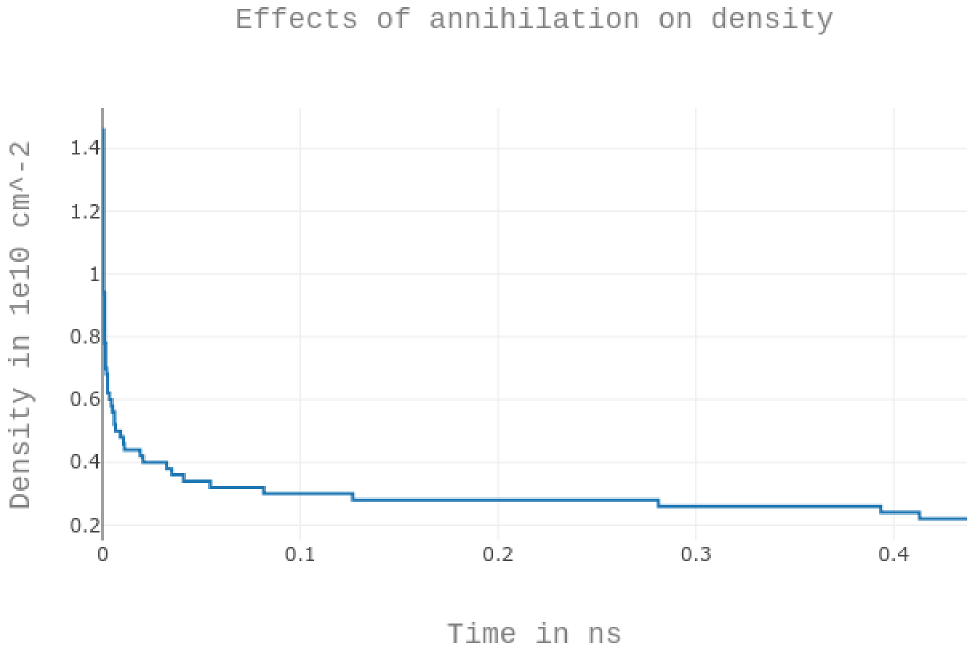

Figure 3.1: Density of charge carriers in a periodic boundary condition (see Subsection 3.3) setting if we allow for annihilation of pairs. In this particular example the pairs were annihilated if respective distance was smaller than the cut off distance r_{cut} and their total energy was sufficiently negative. The rate of annihilation is high in the beginning but as the density drops it slows down. We can understand this effect - as the density of particles becomes lower the average distance between particles becomes bigger. Therefore, e-h pairs will come close less often.

Therefore we need a "hands-on" physical approach in order to ensure the stability of numerical time integration. Since e-h pair tend to get close to each other, one would naively like to let the pairs recombine whenever they come within some distance from each other (r_{cut} - that is, annihilate them both by creating an phonon and photon to carry the resulting momentum and energy. However, within the framework of this simulation this will cause energy loss - we don't simulate any particles except for the charge carriers.

However the main issue with this approach is enormous resulting rate of annihilation. Typical annihilation time in graphene is somewhere around 150 – 400 ns [22]. Figure 3.1 tracks number of particles in a graphene box where we allow the annihilation of particles. The typical timescale of annihilation we observe is many orders of magnitudes higher than the physical expectation.

The interpretation of this fact is quite straightforward - it is not enough to be "close" for pairs to recombine. The actual annihilation mechanism is more involved and beyond the scope of this work. We propose a different mechanism in order to deal with the stability issues due to e-h pairs. Most pairs of particles would simply move around each other, gaining momenta and then move away with huge kinetic energy. Since the numerical integration diverges from physical trajectories in these cases we need to "collide" the pairs "by hand". This process happens when two particles are r_{cut} away from each other with relative velocity that will make the pair closer together. The kinetic energy, momentum and angular momentum are all conserved in this approach. In order to conserve the angular momentum we are forced to change only the momentum parallel to the distance vector between the respective particles. The exact expression can be found in Appendix B.

Physically the pair would move away from each other and interact with other charge carriers in the system - effectively "forgetting" the bond with it's counterpart. In typical graphene systems it is believed that no strong bonds will form due to this effect. However, in our implementation a particle does not gain an enormous amount of kinetic energy by orbiting it's partner - and therefore is unable to move away (spatially) from it's counterpart and interact with other particles. Particles might remain bounded to it's counterpart due to this effect. To avoid this unphysical phenomena we set the force between the two particles to zero for one iteration after collision. This ensures that the strong bounds break but it also cases a spike in energy in the next iteration as the potential energy reappears. Theses spikes are local (in time) and we can give the worst case change by imagining a situation where two particles were going straight at each other and then got turned away. Then their distance will increase by $2\Delta t$ and we can write:

$$\Delta V = -\alpha\left(\frac{1}{r_{cut}+2\Delta t} - \frac{1}{r_{cut}}\right) = \frac{2\alpha\Delta t}{r_{cut}(r_{cut}+2\Delta t)}. \tag{3.3}$$

Note the sign of the change - it is positive therefore the energy of the pair moves towards the positive values.

The real-space cut off r_{cut} becomes the second parameter controlling the stability of the numerical scheme. In order to have a physical description at certain length scales (for example l_{ee}) we need r_{cut} to be way smaller than than this length scale. This increases computational effort as the Δt parameter needs to be lowered if r_{cut} becomes lower in order to ensure stability (and approximate energy conservation). Therefore more iterations are needed and thus more computations. Finding the right balance between these two parameters will be done empirically and will be presented as part of the results in the Section 4.1.

3.3. Boundary conditions

If one is interested in the bulk properties of a material (such as correlation time, viscosity and energy-distributions) one would like to simulate a big, roughly uniform system. We approximate that by simulating a test volume and stating that general neighbourhood of this bulk volume mirrors the test volume - making the periodic boundary conditions (PBC). Another mechanism used to simulate the neighbourhood of the test volume is to keep track of so called nearest image convention. When computing particle-particle interactions between particle A and B we need to "copy" the test volume 8 times - one for each possible neighbours of our (rectangular) test volume. This gives rise to interaction between A and B, B', B''... etc. We keep only the interaction with *nearest* image of B. One can think of it as simulating not a "test volume of N particles" but rather "N test volumes centered at each particles". It might seem like very expensive operation - 8 times more calculations at least. However, as it turns out it is quite cheap as we only need to find the distance in the frame centered around the particle A. For a rectangle $(L \times W)$ system we simply need to compute:

$$\mathbf{r}_{AB} = \begin{pmatrix}\Delta x\\ \Delta y\end{pmatrix} \rightarrow \begin{pmatrix}\Delta x + L/2 \mod L\\ \Delta y + W/2 \mod W\end{pmatrix} - \frac{1}{2}\begin{pmatrix}L\\ W\end{pmatrix}. \tag{3.4}$$

Note that we can choose to make the system periodic in only one direction too. This implementation of periodic boundary conditions conserves the momentum and energy (due to Eq (3.4)) but it does not conserve angular momentum (as the boundaries move particles w.r.t. the test volume).

In order to simulate transport however we need a system describing a physical device. In particular, the boundaries used in analytic approaches [19][18][16] have big influence on the physics near the boundary.

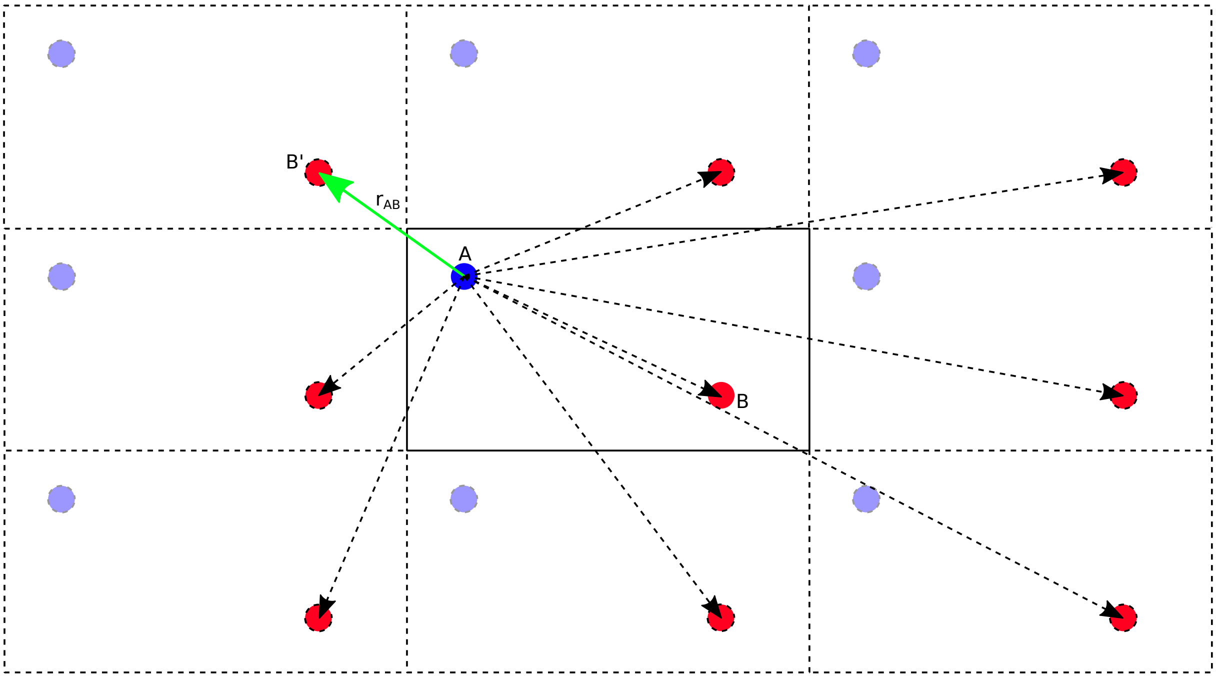

Figure 3.2: The concept of the Nearest Image. The dotted lines represent "copies" of the original system in the middle. We define the distance vector between A and B to be the shortest distance between A and one of the mirrors of B. Here it's shown in green. Note that while the Eq (3.4) ensures smooth changes in the magnitude of the potential it might cause huge changes in the direction of the force.

Two different approaches are the hard-walls and no-slip boundaries. Both are ways of modeling the end of graphene - an area where the charge carriers can't go - be it an insulator or simply vacuum.
The hard walls approach is to enforce no flux through the boundary. Naively, this can be done by simply bouncing the particles as they hit the boundary - that is to change the momentum orthogonal to the boundary to point away from it the moment the particles touch the boundary. Conservation of kinetic energy is trivial to show as the bounce is just a change $k_\perp \to -k_\perp$ but if we let the wall simply move the particle back into the system we will change it's potential energy - changing the potential energy of all particles in the process. We propose a different approach that will still keep particles inside of the system but won't change the potential energy directly. We let the particles escape the system - and then flip their momenta only if they are outside the the system and if their current velocity points away from the system. That way no particles potential energy is changed by the boundary (therefore conserving total energy). The hard wall now has a thickness of about Δt as particles can travel "outside" of the system for an time step.

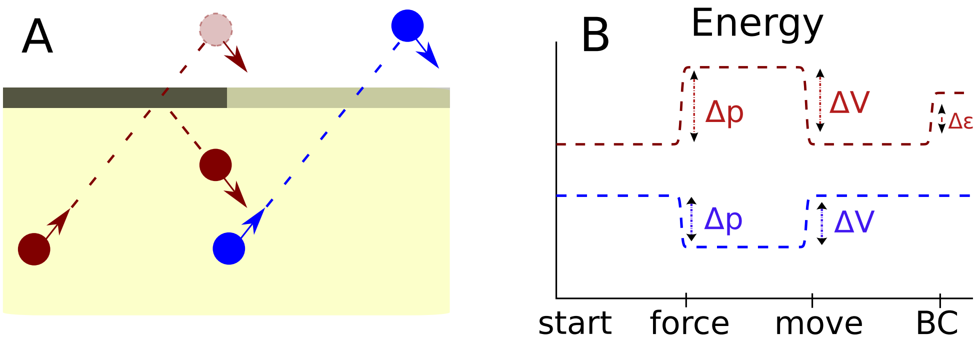

Figure 3.3: Example of two possible implementations of hard wall BC. In Figure A we see the trajectories of particles approaching the hard wall. On the right (red) we see a typical implementation of hard wall - a trajectory that gets reflected by the wall both in momenta and position. The left (blue) particle will go through the boundary but only it's momentum will get reflected by the wall. This ensures the particles return into the system and thus the this BC does *keep particles inside of the system.* In Figure B we see corresponding changes in total energy. Both particles move according to Eq (3.2) however for the red case the hard wall applies a force onto the particle by pushing it back into the system (therefore moving it w.r.t. potential field of other particles).

The second condition - the no-slip condition - ensures zero velocity on the boundary and meant to model particles being "stuck" to the boundary of graphene edge. Within the context of Molecular Dynamics it is hard to model a fitting algorithm ensuring this behaviour. In particular, it is not possible to simulate the mechanism responsible for the slow down as the edge states in graphene do indeed move slower [23] due to different dispersion relation. Directly changing the dispersion relation of the particles near the system edges would be complex and (computationally) slow process. Luckily this effect decays quickly as we move away from the boundary so we will focus on physics that don't require this phenomena to occur.

3.4. Leads

In order to make transport simulations possible we need to discuss a special boundary condition - the lead. Leads allows us to inject particles into the system in order to change the chemical potential of the system or apply a potential difference to the particles inside of the system. In the first case we compute injection rate per iteration N_{inject} as:

$$N_{\text{inject}} = \left(n_h\left(\mu, T\right) + n_e\left(\mu, T\right)\right) \times W_{\text{lead}} \times \Delta t, \tag{3.5}$$

and inject particles according to distribution given by the product of Eq (2.4) and Eq (2.5). The particles can also leave the system - if they go into the lead. The injection of particles will clearly change the number of particles - and this is a computationally challenging as the memory allocation needs to change often in order to keep track of the particles. In order to simplify the computational effort we propose a method that will simulate charge flow but will keep the number of particles constant. Whenever a particle goes into the lead, a new particle will appear on the other side of the lead - therefore fixing the number of particles. Note that this approach doesn't generalize to system with multiple leads.

The charge and kinetic energy is determined using a non-interactive dispersion therefore it does not necessarily obey the kinetic energy distribution of interactive particles (see Section 2.3). The physical properties of particles entering the system will thus differ from real properties of charge carriers in hydrodynamical graphene. Furthermore, charge appearing at the edge will change the potential energy of particles near it. Therefore we need to realize that, within the framework of this simulation, the region near the leads will always be perturbed. It is hard to specify any characteristic length scales for this propriety a priori but we will see an approach to deal with this unknown in Section 3.6.

Note that we can put different leads at different biases. This bias difference can be translated into an applied voltage $\mu_{\text{bias}} = eV_{\text{bias}}$, which we further translate into an electric field $E = \frac{V_{\text{bias}}}{L}$. We can thus apply an extra force to the particles in the system in order to simulate voltage bias - an essential tool needed to investigate I-V properties of the system. It is also possible to set the leads to different temperatures, in order to simulate charge current through temperature gradient mechanism - but there is little to no way to enforce smooth thermalization within the system. Therefore, we have no real way of simulating continuous temperature gradient through a graphene sample.

Measurements of current are done by counting all charge flow crossing some line over time. Typically, this value will oscillate significantly due to shot noise so we need to average these signals in order to achieve a reasonably consistent results. Furthermore, measuring current near a lead will result in bigger oscillations of instantaneous current as the particles are very likely to go back and forth through a current line. By repeating the experiment and averaging the results a consistent value is obtained.

3.5. Geometries

Within the framework of molecular dynamics simulations, creating a hard wall constriction (see Figure 3.4) results in a mechanism to relax momentum along the channel (p_x). It is expected that current flow near the edges of such constriction will create vortices [11] which would be observable in our simulations. Such vortices haven't been studied extensively (other than the fact of their possible existence).

One can imagine that the constriction is a major source of resistance in the system. Therefore if a particle starts crossing the constriction its very likely to actually contribute to the current through the whole device (as opposed to drifting back and forth as happens in the non constricted bulk more often). Therefore the current measurements in the narrowing will have lower variance (variance in this sense refers to the oscillations of the instantaneous current). Lastly, more interactions between particles means that near the narrowing the charge carriers will approach the local equilibrium quicker. This helps with the perturbations caused by the leads.

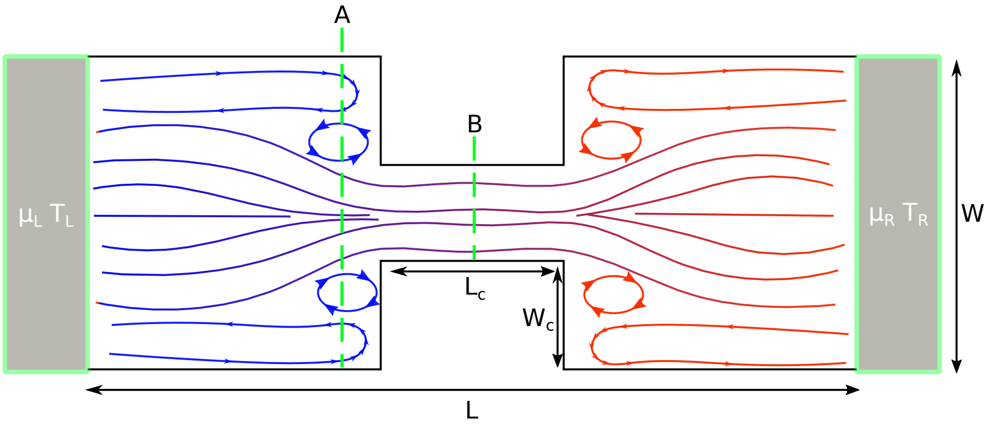

Figure 3.4: Our proposed experimental geometry consists of two leads of width W and distance L apart, kept at different μ and/or T. In between the leads a scattering region is introduced - the constriction of dimension $L_c \times W_c$. We show typical flow pattern - top and bottom regions will create bounded states as charge carriers come out of lead with high momenta in the direction along the channel, scatter of the constriction and travel back towards the lead. The middle region will feature highly perturbed flow as some particles from the top and bottom parts of the junction will funnel into the constriction opening. It is possible that vortices will appear near the edges of the channel - but they will not necessarily be symmetric and/ro at both sides of the constriction. This is definitely an effect depending on the actual properties of the flow. Lastly, lines A and B show examples of reference lines to keep track of the current between the leads. Note, however, that each charge traveling through line B contributes to total current in this flow diagram while crossing of line A might be very noisy because of the vortexes and bound states appearing away from the constriction.

3.6. Physical observables as functions of spatial coordinates

Within the framework of MD simulation one often uses the principle of ergodicity, essentially stating that we can interchange *ensemble* averages with *time* averages. This allows us to use the time-evolution in order to compute physical quantities such as viscosity and energy distribution. As we have seen we are building towards measuring quantities that occur in specific places, namely away from leads, near the borders of constriction and within the constriction itself. Therefore the framework used to computed *local* quantities, such as density or current, is introduced in this chapter.

The simplest approach would be to define a grid and bin all the particles according to their positions. Each physical quantity A can be then locally calculated by computing $\sum_{\text{particles}} A_p \delta\left(\text{particle in the bin}\right)$ for each of the bins. Let us consider density of particles ρ (so $A = 1$). A high resolution image of local properties would require numerous (and therefore small) grid cells. If the size of grid cells becomes comparable to particle-particle distance then the cells are so small that slightly changing the position of a particle will change the value of local density in the grid point and it's neighbour significantly thus creating a big variance between sites and resulting in noisy plots. In Appendix C we investigate this concept in more detail.

The idea is to change the delta-peak like contribution of a particle towards the local quantity. An averaging method is introduced by changing it to an integral over a Gaussian peak with standard deviation σ and mean equal to the position of the particle, so that the local value of variable A at grid point i becomes:

$$A_i := \frac{\sqrt{\pi\sigma^2}}{2\sqrt{2}V} \sum_{p\in\text{Particles}} a_p \left[\operatorname{erf}\left(\frac{x_p - x}{\sqrt{2\sigma^2}}\right)\operatorname{erf}\left(\frac{y_p - y}{\sqrt{2\sigma^2}}\right)\right]_{\text{grid}_i} \tag{3.6}$$

where the V is the volume of a bin. The only free parameter σ is chosen to be a fraction of the p-p distance l_{pp}. Physically one can think about it as the wave function of charge carriers being constrained to an area of roughly l_{pp}^2. This way the variance between neighbouring sites will be substantially lower and a higher signal to noise ratio will be obtained.

Noteworthy the resolution of this procedure can be improved while lowering the cost of calculating the value. Prior, we needed to calculate the density of each particle and sum it, therefore the calculation scales as $\mathcal{O}\left(N_{\text{particles}} \times N_{\text{grid points}} \times N_{\text{timesteps}}\right)$. Now, if we increase the number of grid points such that the distance between two points is on the order of σ we can simply ignore the position of a particle within the grid square (and assume it's on the center of it). The result is the computational complexity of $\mathcal{O}\left(N_{\text{particles}} \times N_{\text{timesteps}} + N_{\text{grid}}\right)$ - a vast improvement.

Finally we would like to present a typical density plot in PBC setting. For this we simulate a small rectangular sample with sides of 5×10^2 nm at $T = 50$K and $\mu = 3.5 k_B T$ (density of $3.5 \times 10^{10}\,\text{cm}^{-2}$). In this setup we expect the density to be constant throughout the system. We use this macroscopic quantity as the benchmark for the method. Figure 3.5 a shows the approximation of the density by data binning. Figure 3.5 b shows the smoothed out density obtained by setting $a_p = 1$ in Equation (3.6). The superiority of this approach can be understood by looking at Figure 3.5 c showcasing the relative std between two methods.

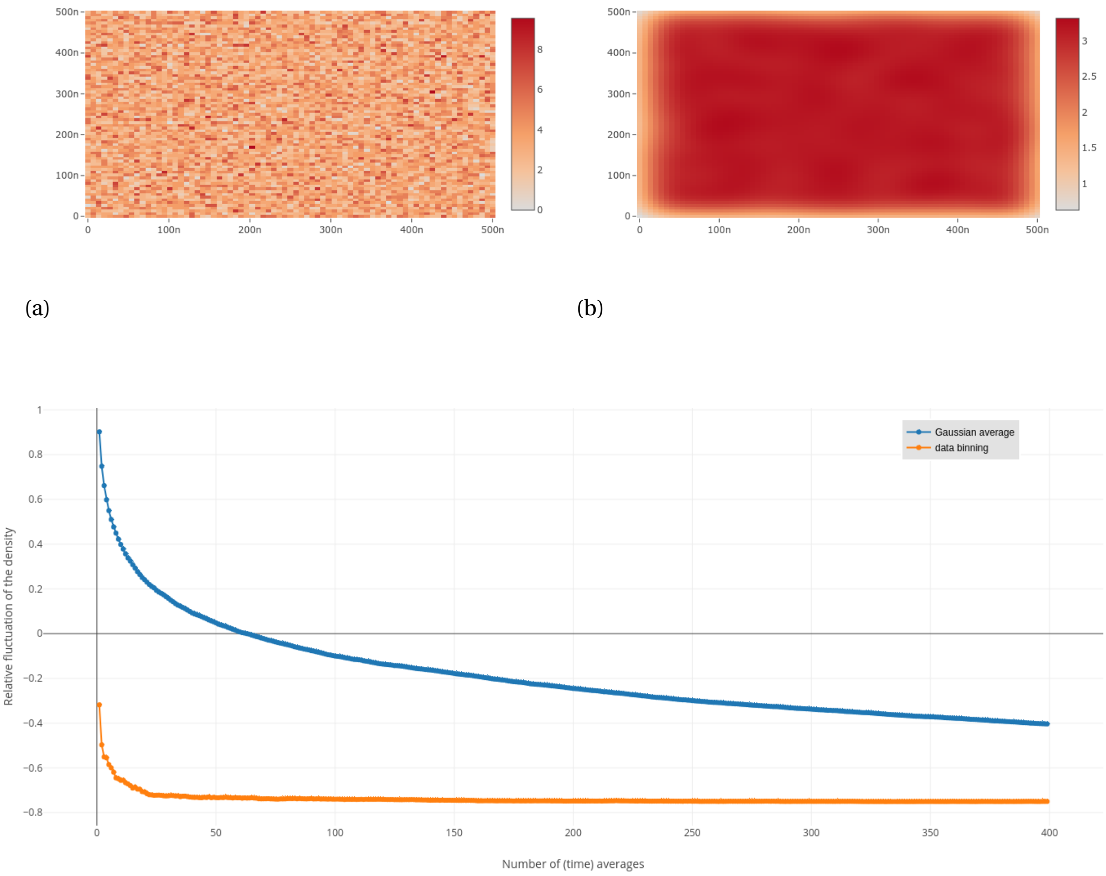

(a)

(b)

(c)

Figure 3.5: (a). The approximate density obtained by binning of particles averaged over 400 samples, as a function of position within the system. The color map is in units of $1 \times 10^{10}\,\mathrm{cm}^{-2}$. The magnitude of density varies w.r.t. its nearest neighbour, making the plot very noisy. Furthermore, we observe big variance with respect to the expected value of $3.5 \times 10^{10}\,\mathrm{cm}^{-2}$. (b). Approximate density of particles obtained by Gaussian smoothing, averaged over 400 samples, as a function of position within the system. The color map is in units of $1 \times 10^{10}\,\mathrm{cm}^{-2}$. The expected value of density in the bulk corresponds to the actual density in the system, while near the boundary it drops off. This is due to smoothing procedure not handling the periodic boundary conditions in the computations. (c). The variance between the grid points relative to the (approximated) mean value of the density, on a logarithmic scale as a function of the number of samples. We see a quick drop of variance for both approaches but Gaussian smoothing begins and remains orders of magnitude better. Furthermore, the leveling off of the variance has to do with improper handling of the grid points near the boundary of the system, effect irrelevant in physical systems where we work with hard walls.

4

Results

4.1. Stability of the numerical approach

In this section the optimal choice of stability-controlling parameters Δt and r_{cut} is reported. We handle the case of Dirac and Fermi fluids separately, since the two regimes vary vastly. Both simulations are done in rectangular PBC setups and on timescales orders of magnitude longer than l_{pp}. Two observables are crucial here: the lack of energy drift on long time scales and small fluctuation of the energy. Two metrics are used, we report on total energy of the system after a long time and the typical fluctuations relative to the total energy. The energy is expected to grow over time if $\frac{\Delta t}{r_{\text{cut}}}$ gets above some threshold and the fluctuations increase whenever r_{cut} grows as per Eq (3.3). Note that these results will change as the density within the system changes.

4.1.1. Fermi regime

All of the results in this section were done at $T = 50K$, $\mu = 100K$, $N = 124$ and a density of $1.9 \times 10^{10}\,\text{cm}^{-2}$. First we present behaviour of the total energy of the system on long timescales. Some choices of parameters lead to divergence of the energy, leading to nonphysical results.

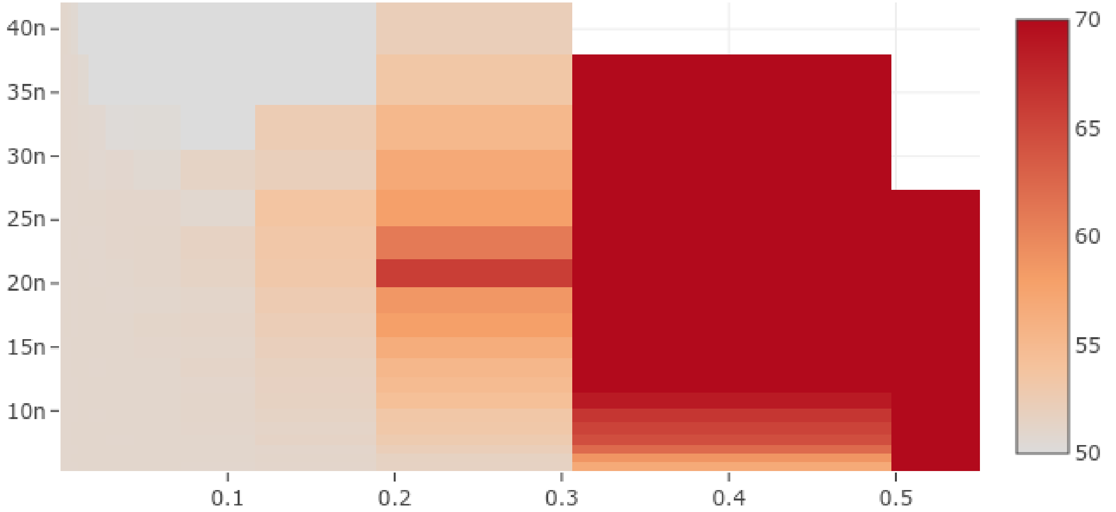

Figure 4.1: Total (average) energy as a function of r_{cut} on the y axis and $\frac{\Delta t}{r_{\text{cut}}}$ on the x axis. We cut the values off at 70 and 50 (in arbitrary units), therefore all the deep red correspond to energy escalating due to instability. White empty space corresponds to NaN value due to overflow. The area left of $\frac{\Delta t}{r_{\text{cut}}} = 0.3$ remains within the bounds of the energy. One can observe how changing the stability parameters changes the physical properties of the system, in this case the total energy is slightly higher between $\frac{\Delta t}{r_{\text{cut}}} = 0.2$ and 0.3. Seeming lack of dependence on the r_{cut} in the stable part of the plot suggest that particles never come within the distance of 40 nm within the simulation.

Secondly we report the fluctuations of the energy in time. Big fluctuations can be a sign of the conserved pseudo Hamiltonian not being close to the original Hamiltonian of the system Eq (2.3). In order to understand why energy oscillations appear we urge the reader to see Appendix B.

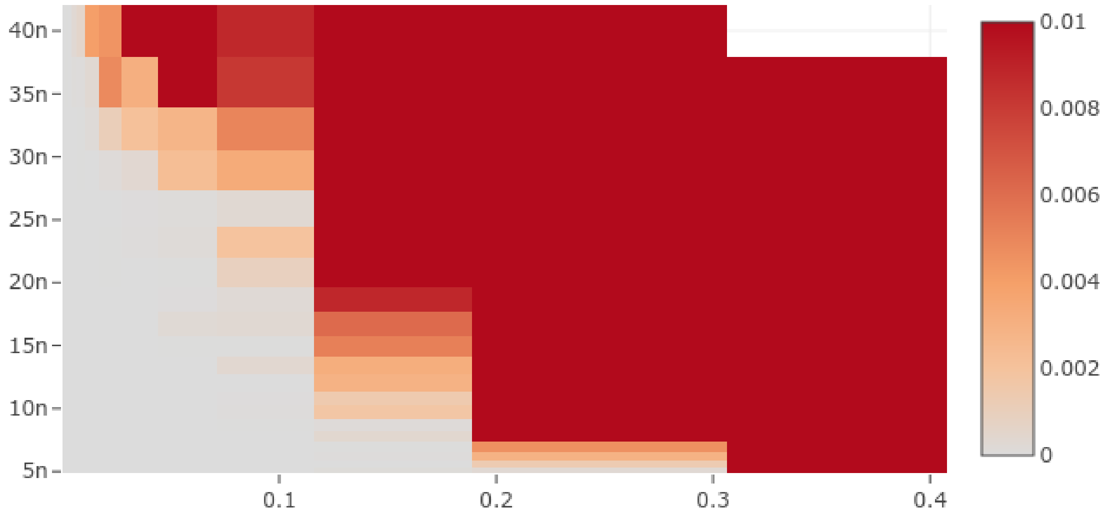

Figure 4.2: The relative fluctuations in total energy due to numerical approximation as a function of r_{cut} on the y axis and $\frac{\Delta t}{r_{\text{cut}}}$ on the x axis. We cut off all of the values at 1% margin in deep red. There is a sharp interface between fluctuating and non fluctuating regions. We can observe a roughly linear relation between r_{cut} and $\frac{\Delta t}{r_{\text{cut}}}$ marking the boundary. All of the grey point are left of $\frac{\Delta t}{r_{\text{cut}}} = 0.3$ and therefore are valid simulation parameters. Above the boundary simulations fluctuate more abruptly. This is caused by bigger Δt creating bigger difference between discrete trajectories and continuous ones.

We observe a large triangular region of stability in terms of r_{cut} and $\frac{\Delta t}{r_{cut}}$. The outermost stable points are $r_{cut} = 40\,\text{nm}$, $\Delta t = 3.8\,\text{fs}$ and $r_{cut} = 7\,\text{nm}$, $\Delta t = 1.5\,\text{fs}$ allowing us to vary r_{cut} according to specific needs while keeping the time step reasonably high.

4.1.2. Dirac regime

The simulations were performed at $T = 100$, $\mu = 0$, $N = 95$ and a density of $1.5 \times 10^{10}\,\text{cm}^{-2}$. The reasons for showing these plots are the same as in previous section and therefore won't be restated.

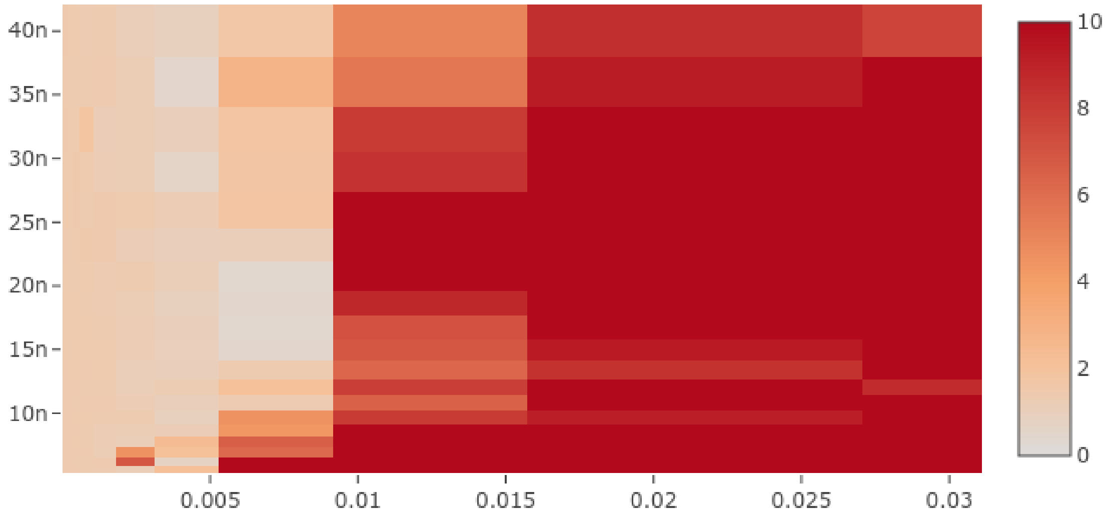

Figure 4.3: Total (average) energy as a function of r_{cut} on the y axis and $\frac{\Delta t}{r_{\text{cut}}}$ on the x axis. We cut the values off at 10, therefore all the deep red correspond to energy escalating due to instability. Note the difference w.r.t. the previous subsection, all of the energies are vastly lower due to the negative potential. The values of Δt are vastly lower compared to the previous section, left of $\frac{\Delta t}{r_{\text{cut}}} = 0.01$ the values of energy don't seem to diverge although one needs to be aware of some instability for low r_{cut} visible in that region.

In Figure 4.3 we observe a breakdown of the stability at combinations of r_{cut} and Δt that would be stable in Fermi regime. The magnitude of the p-p potential at r_{cut} is exactly the same for both cases therefore it must be the sign of the potential causing it. It is unclear if this effect is due to particles not reaching the distance r_{cut} when the potential is positive or due to error terms canceling out for the negative case.

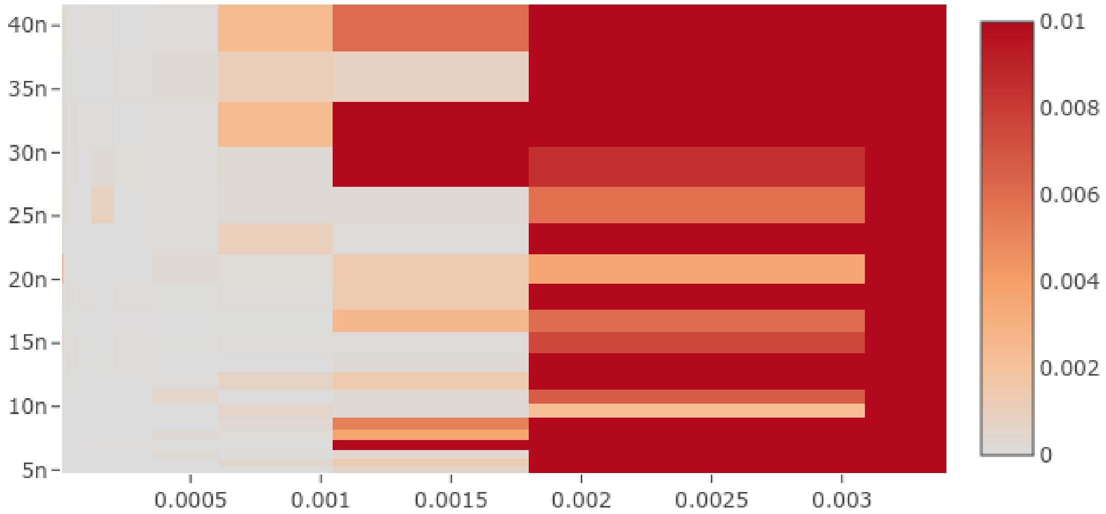

Figure 4.4: The relative fluctuations in total energy due to numerical approximation as a function of r_{cut} on the y axis and $\frac{\Delta t}{r_{\text{cut}}}$ on the x axis. We must focus on a much smaller region than the Figure 4.3. There are two effects at play causing this behaviour, both of them originating in negative potential domination. First the total energy is lower compared the Figure 4.1 and therefore the fluctuations are more pronounced. Second, e-h interactions attract particles together, causing bigger fluctuations as can be seen in Eq (B.6). One can speak of low fluctuations for data points left of $\frac{\Delta t}{r_{\text{cut}}} = 0.0015$ and there is not a clear boundary for the regio.

We observe far more stringent constraints on Δt. In particular, one needs to look at values 2 order of magnitude lower than in the case of the Fermi regime. Also, the energy of the system varies more as a function of r_{cut}. The stability region is less well defined, but we can postulate values of $r_{\text{cut}} = 5.6\,\text{nm}$, $\Delta t = 11.5\,\text{as}$ and $r_{\text{cut}} = 25.8\,\text{nm}$, $\Delta t = 91.7\,\text{as}$ as possible candidates for simulations.

4.2. Viscosity effects

In this section spatial charge velocity correlations are shown. The simulations are done in the Dirac Fluid regime and are meant as a qualitative arguments rather quantitative description of phenomena shown. Due to restrictions on the time step shown in last section it was not feasible to simulate charge transport over any sufficient time scale. However, we were able to simulate for times long enough to obtain consistent local values (see Section 3.6) of particle and charge density and velocity. Figure 4.5 shows a variety of rich physical phenomena that can be probed in this regime. All of the plots were made in a constriction geometry (as seen in Figure 3.4).

4.3. I-V characteristics at high bias

In the Fermi regime it becomes possible to simulate long enough for transport to equilibrate. All experiments in this sections were done in a constriction geometry shown in Figure 3.4 with: spatial dimensions $L = 1.2\,\mu\text{m}$, $W = 500\,\text{nm}$, $L_c = 200\,\text{nm}$ and $W_c = 150\,\text{nm}$, stability parameters $\Delta t = 500\,\text{as}$ and r_{cut}. We set the leads to 50K and a chemical potential of $15\text{meV} \pm eV_{\text{bias}}$ with negative voltage for left and positive voltage for the right lead. We will vary the bias voltage (with a maximal bias of $eV_{\text{bias}} = 3\text{meV}$) in order to simulate transport. Each simulation has been done multiple times, starting from the same initial condition but with a different random seed in order to approximate the variance due to randomness.

4.3.1. Typical particle drift velocity

We start by showing typical density and velocity in the x direction distributions. In the Fermi regime the charge carrier density and drift velocity v_{drift} directly relate to current via $j = nev$ so these macroscopic quantities are a good first approximation for the current expected. We start by showing a result for $eV_{\text{bias}} = 6\mu\text{eV}$ in Figure 4.6. Afterwards we focus the attention on effects of bias voltage. The idea is that applying electric field will force the flow to go through the constriction. Figure 4.7 shows the effects that external applied electric

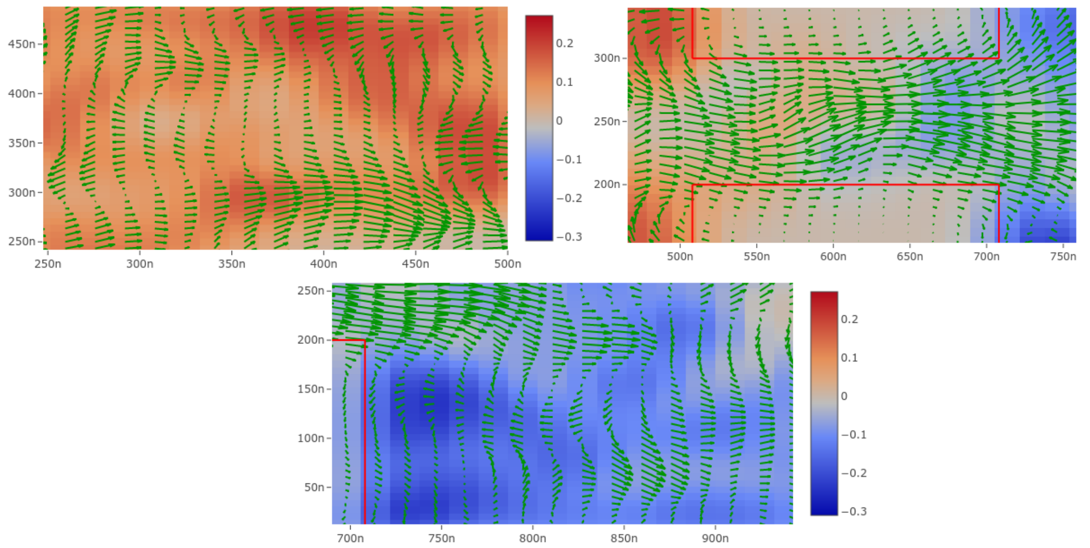

Figure 4.5: Top left corner: charge drift velocity near the entrance of the constriction. The flow in the on the bottom of the plot becomes bigger as we approach the entrance. Towards the right upper corner we can see effects of viscosity, as the current into the constriction slowly changes sign due to the hardwall boundary. Effects of long range correlations can be observed in the sign flipping of the current on the left side of the plot. Top right corner: charge drift through the constriction with a background of the charge imbalance. In this setup an voltage bias was applied forcing the charge carriers to travel coherently through the constriction. We can see typical Poiseuille flow velocity profile within the constriction. Note the slight funneling effect around 600 nm. It occurs correlates with a slight local charge imbalance. On the edges of constriction we can see boundary effects changing the flow. Bottom corner: charge drift near the exit of a constriction. The background is the local charge imbalance. We see negatively charged region, with a vortex trapped inside of it. Viscous forces of the current around it push the charge carriers towards the inside of the vortex, canceling out the repulsive forces between particles in the vortex.

field has on the current flow.

4.3.2. Conductance correlation at different bias

We investigate the conductance of the constriction channels in more structured way by considering the behaviour of conductance correlation. Usually one investigates the current correlation but for fixed voltage (as in our case) the two differ by a prefactor only. In equilibrated system the correlation should drop exponentially with some characteristic time scale $t_{\text{correlation}}$. Figure 4.8 contains the conductance plots and correlation as a function of time for systems discussed in previous section.

4.3.3. Viscosity and conductance correlation

Lastly we show values of viscosity (computed as per [15]) calculated away from leads between $x = 0.2\mu$m and $x = 1\mu$m and compute the conductance from hydrodynamical theory Eq. (2.11). Value of conductance determined by counting charge passing through the constriction is also shown in Figure 4.9. The errorbars are obtained by calculating standard deviation between different realizations of the same simulation.

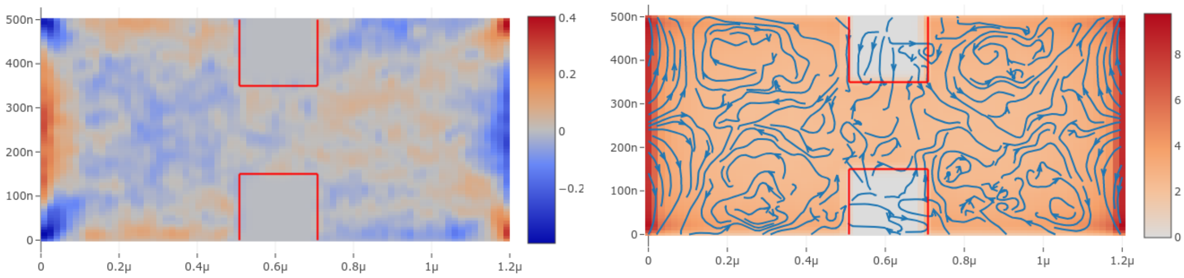

Figure 4.6: Subplot a: Drift velocity within the sample. Unexpectedly we observe the velocity change sign 4 times in between the leads. The value of drift velocity changes slowly within the constriction but near the leads we see an abrupt sign flip. The middle of the lead pumps particles into the system and the top and bottom suck it out. The velocity profile is roughly symmetric around the middle of constriction. Subplot b: Flow diagram of the system with a background of density in units of $1 \times 10^{10}\,\mathrm{cm}^{-2}$. Indeed, near the leads the particles go in circular motions. As described in Section 3.4 the leads keep the density in the system constant by moving particles leaving through it to the other lead. This explains the closed loops forming near the lead, as particles go into the system, bounce of the bulk density at around $x = 0.2\mu$m and $x = 1\mu$m, return into the lead and repeat the same procedure on the other side of the system. For this reason we see a higher density near the leads. However, the bulk of the system has constant density, implying that the flow separated into a section around leads and a section around the bulk of the system. Each of these sections prevents mixing with the others via applying pressure. The sections don't collapse under this pressure most likely due to internal pressure caused by the bouncing approach and hardwalls. Flow within the bulk is very noisy and chaotic. There is little to no flow through the constriction, as opposed to the expectation. Lastly, note that the flow-lines outside the bounds of the constriction are simply a by product of quiver plotting procedure. On the plot a we can see extremely low values of velocity there, as it should be since it is empty.

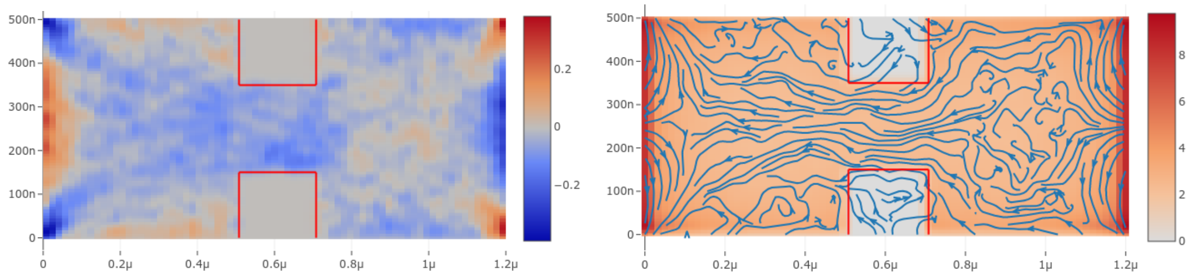

Figure 4.7: Subplot a: Drift velocity within the sample at $eV_{\mathrm{bias}} = 3$meV. We see again the sharp sign changes near the leads but now the drift is clearly more pronounced in the bulk, especially in the constriction. It is possible to observe Y shaped flow within this sample. Subplot b: Flow lines with a density background. We indeed see coherent flow through the constriction. Again, the effect of closed loops on both sides of the leads persists. Notably the area where both flows meet, $x = 0.2\mu$m and $x = 1\mu$m moved to the left by about 0.01μm. It is best to redefine thermalized system to be between these two lines and consider the rest of it as larger leads. Near the right entrance of the constriction we can see effects of viscosity in the shape of current "hugging" the wall as in goes into the constriction. On the left side however, we see vortices appear due to interaction between inter-particle forces and boundary conditions. The density within the system is roughly constant in the bulk and elevated near the leads. We expect higher current through this device as the drift velocity in the constriction is higher.

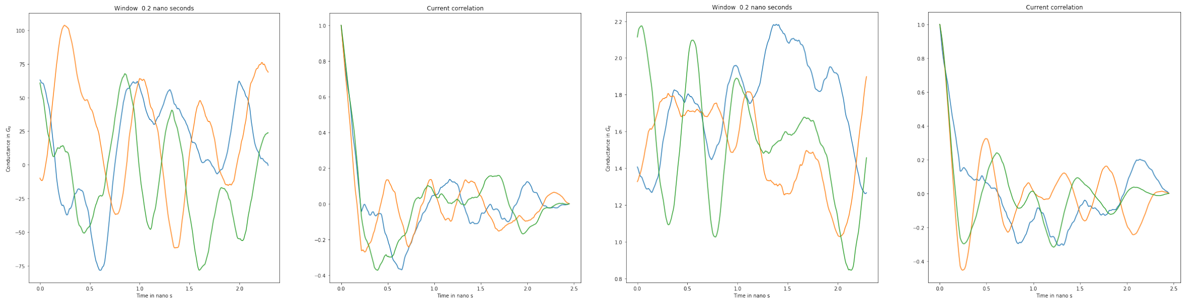

Figure 4.8: Subplot a: the conductance at low bias voltage for multiple random seeds as a function of time. We observe enormous fluctuations of conductance and the sign changing. This is unexpected behaviour, as we expect the conductance to remain around zero for the low bias device. One possible explanation for this is the system equilibrating to a state where two charge densities bounce of each other, one going into the lead and arriving at the other side and the other traveling through the constriction to the other side where the process repeats. This phenomena would cause big (and sign changing) fluctuations in the charge transport through the constriction. Subplot b: conductance correlation for multiple realizations as a function of time supports this phenomena. We see an quickly dropping correlation followed by a oscillation. Oscillations in the correlation function are a sign of system not equilibrating. Subplot c: the conductance at high voltage for multiple realizations. We see stable conductance with small oscillations. It is questionable why the conductance is this low however. Value of few conductance quanta is expected out of quantum dots and not nano sized channels. Subplot d: conductance correlation at high bias. We again see oscillations in the correlation, related to the behaviour near the leads.

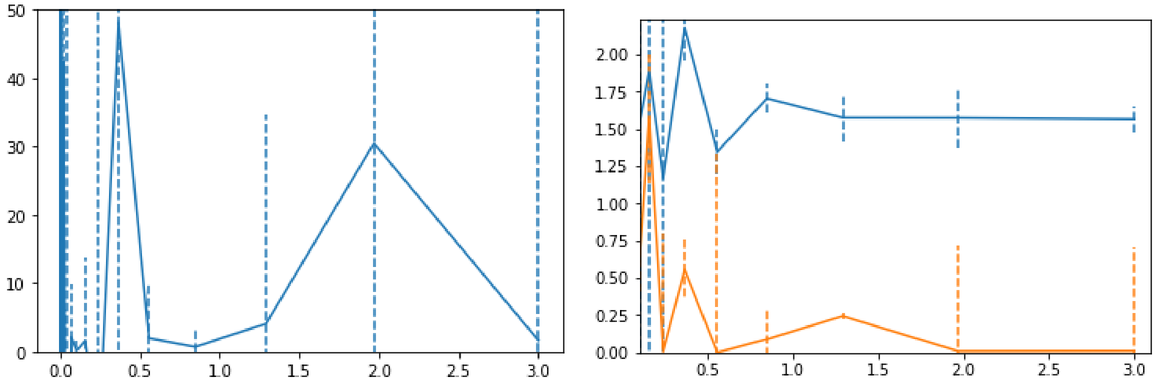

Figure 4.9: Left: The viscosity (units of Pascal second) of charge carriers within graphene as a function of applied bias voltage (in the units of meV). The value is in the right order of magnitude [5], for comparison honey has a viscosity of about 10 Pa s. However, the uncertainty in the data points and general lack of coherence between data points forces us to conclude that this statistical property can't be derived from our model as postulated. Right: Conductance of the channel in terms of conductance quanta. Orange line is the theoretical prediction from hydrodynamical theory, based on the viscosity calculation. Given the values found for viscosity we do not expect this curve to be right. We again see values smaller than the standard deviation error. Blue line is a result from straightforward computation of the charge passing through the constriction. One can observe consistent values with small errors at high bias. At low bias the error again becomes bigger than the value. It is noteworthy that the pattern of minima and maxima of both curves (at low bias) coincides. It is reasonable to speculate that poor perfomance of both methods (viscosity calculation and counting of charge) has orgin in exactly the same phenomena.

5

Conclusion

In this work we have presented a model of Coulomb interactions between charge carriers of graphene. We have shown the importance of incorporating this potential energy scale when considering charge carriers at low and high chemical bias μ. By considering the statistical properties of Eq 2.1 we understood the effects adding Coulomb interaction will have. Specifically have characterized two different regimes within hydrodynamical graphene, the Fermi Liquid regime with $\frac{\mu}{k_B T} \gg 1$ where charge carriers are of the same type and the potential energy is positive and the Dirac Liquid regime $\frac{\mu}{k_B T} < 1$ where the charge flow consists of electrons and holes and the interaction is attractive, making the potential negative. Proper energy dispersion in the presence of interactions is an open question theoretically.

We simulated the dynamics of our model in the framework of Molecular Dynamics approach using the sympletic Leapfrog algorithm. The diverging Coulomb potential proved to be problematic numerically, leading to development of bouncing mechanism characterized by a length scale r_{cut}. The parameter r_{cut} became the second parameter ensuring stability and lack of long time energy drift of the system, next to timestep Δt. Physical devices have been modeled in terms of boundary conditions and ways to bias the system. We have introduced a creative approach for calculating local physical (single particle) observables such as density or drift velocity. The approach has been shown to converge quickly to proper macroscopical average of relevant quantities.

The main result of this work are the stability analysis of the Leapfrog method for this particular potential and the display of long range correlations between particles. We find the Dirac regime to require very low Δt in the order of tens of atto seconds. The Fermi reqime performs orders of magnitude better by remaining stable at timestep of few femto seconds. We were able to show the velocity of change signs as a result of viscous interactions both in Fermi and Dirac fluids. However, statistical-physics based methods used to compute viscosity and current did not perform well. The outcomes of experiments are subjected to substantial deviations, therefore it was impossible to reproduce any physical properties reported in literature. Furthermore, the system did not reach a thermal equilibrium due to non-interactive energy dispersion of the leads.

The conclusion forces itself: modeling of specific devices by addition of leads introduces perturbation big enough as to make full thermalization impossible. However the parts of the project working well, that is computation of time evolution of the system and describing the macroscopic properties of the system within just few timesteps open the door to a different approach. The idea is to implement random sample generation in hybrid Molecular Dynamics - Monte Carlo algorithm. This approach lets the system evolve in a MD fashion for short times (long enough to gather information about local observables however) and then introduce random perturbations to the system, followed by thermalization time period. The perturbation can be chosen in such a way as to simulate transport via averaging over local perturbation response properties leading to a novel approach to transport simulations.

A

DoS derivations

A.1. Structure of graphene

A.1.1. Lattice structure

Graphene is a 2 dimensional material consisting of carbon atoms in a honey-comb structure. The displacement between two neighbouring atoms given by:

$$\begin{aligned}\mathbf{e_1} &= \pm a\hat{\mathbf{x}},\\ \mathbf{e_2} &= \pm a\frac{-\hat{\mathbf{x}}-\sqrt{3}\hat{\mathbf{y}}}{2},\\ \mathbf{e_3} &= \pm a\frac{-\hat{\mathbf{x}}+\sqrt{3}\hat{\mathbf{y}}}{2}.\end{aligned} \tag{A.1}$$

With a the atom-atom distance equal to 0.142 nm. The ± sign is due to two different atoms, see Figure A.1. This gives rise to two triangular sub-lattices per unit cell with the lattice vectors $\mathbf{e_1}-\mathbf{e_2}$ and $\mathbf{e_1}-\mathbf{e_3}$. The k−space vectors are easily found by looking for vectors such that the dot product equals an integer multiple of 2π. We come up with:

$$\mathbf{k}_{n,m} = \frac{4\pi}{3\sqrt{3}a}\left(\frac{\sqrt{3}(n+m)}{2}\hat{\mathbf{x}} + \frac{n-m}{2}\hat{\mathbf{y}}\right), \tag{A.2}$$

with n, m being arbitrary integers.

The nearest neighbours are held together by the hybridized sp^2 orbitals. The, in plane, p_x, p_y and s orbitals form σ bounds and remaining, out of plane, p_z orbital forms π bounds. The σ bonds are strong and therefore the electrons in them tend to stay put. As a result theory of transport in graphene is based on nearly free π orbitals creating the π (valence) and π^* (conduction) bands.

A.1.2. Tight binding model

The tight binding model of π and π^* bands is given by hoping terms between the two sublattices (A and B) characterized by energy scale $t \approx 2.8\,\text{eV}$ and on site chemical potential μ describing offset to the charge neutrality point [9]. One should note that nearest neighbours are always on two different sub-lattices so we write:

$$H = -t\sum_{\sigma,<ij>}\left(a^\dagger_{\sigma,i}b_{\sigma,j} + \text{H.c.}\right) - \mu\sum_{\sigma,i}\left(a^\dagger_{\sigma,i}a_{\sigma,i} + b^\dagger_{\sigma,i}b_{\sigma,i}\right), \tag{A.3}$$

with σ the spin $(\uparrow,\downarrow)$ degree of freedom, $< i,j >$ refers to all pairs of nearest neighbours, a and b are creation operators on the A and B sub-lattices respectively. Note that the second term goes over all lattice points. Since each lattice belongs to either A or B one of the terms will always be zero (per definition of an operator acting only on specific sublattice) and the other will simply give us the number of particles at given site. Hamiltonian (A.3) is an example of a Hubbard model Hamiltonian. Methods to solve this kind of problems are well known [20]. After taking the Fourier transform the we can see that the spectrum is simply given by:

$$E(\mathbf{k}) = \pm t|\exp(i\mathbf{k}\cdot\mathbf{e_1}) + \exp(i\mathbf{k}\cdot\mathbf{e_2}) + \exp(i\mathbf{k}\cdot\mathbf{e_3})| - \mu. \tag{A.4}$$

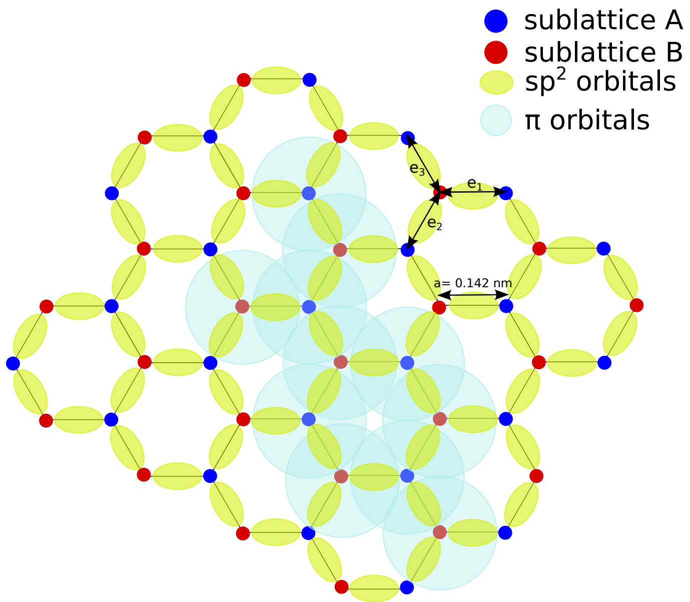

Figure A.1: The crystal structure of graphene. We show the bonding sp^2 orbitals and the conductive π orbital. The π orbital only reaches the nearest neighbour, hence there is no need for a second-to-nearest term in the Hamiltonian (2.1). We show only few of the π orbitals for readability sake.

The charge neutrality point can be found by setting $\mu = 0$ and calculating $\mathbf{k}$ such that the resting term has zero energy. It turns out there are infinitely many solutions to this equation but they are all related to each other by the reciprocal lattice vectors Eq (A.2). Since we have a sublattice degree of freedom we shall state two of the solutions that will be also the lattice points included in the Brillouin zone.

$$\begin{aligned}\mathbf{K} = \mathbf{k}_{1,0} &= \frac{4\pi}{3\sqrt{3}a}\left(\frac{\sqrt{3}}{2}\hat{\mathbf{x}} + \frac{1}{2}\hat{\mathbf{y}}\right),\\ \mathbf{K}' = \mathbf{k}_{0,1} &= \frac{4\pi}{3\sqrt{3}a}\left(\frac{\sqrt{3}}{2}\hat{\mathbf{x}} - \frac{1}{2}\hat{\mathbf{y}}\right).\end{aligned} \tag{A.5}$$

Henceforth the sublattice degree of freedom will be referred too as valley degeneracy. Lets now look at the spectrum near the $\mathbf{K}$ point. Linearization gives:

$$E(\mathbf{k}) = \pm v_F \hbar |\mathbf{k}| + \mu \tag{A.6}$$

with the Fermi velocity defined $v_F = \frac{3}{2} t a \approx 1 \times 10^6\,\mathrm{m\,s^{-1}}$, just a factor 300 lower than the speed of light c.

A.2. Scaling properties

We start by counting charge carriers in the systems as a sum over modes, weighted by the Fermi-Dirac distribution $f(E, T, V)$ where the functional dependence is omitted for sake of readability:

$$\begin{aligned}N = \sum_{k_x,k_y} f = \frac{1}{\Delta k_x \Delta k_y}\sum_{k_x,k_y} f \Delta k_x \Delta k_y = \frac{A}{4\pi^2}\sum_{k_x,k_y} f \Delta k_x \Delta k_y\\ \Longrightarrow n = \frac{1}{4\pi^2}\sum_{k_x,k_y} f \Delta k_x \Delta k_y \approx \frac{1}{4\pi^2}\iint f\, d\left(k_x k_y\right) = \frac{1}{2\pi}\int f k\, dk.\end{aligned} \tag{A.7}$$

In the last step we changed to polar coordinates so k refers there to the norm of $\mathbf{k}$. One should realize that the above expression is valid for *electron* states $E \in [0, 2.5\,\mathrm{eV}]$ - the *holes* $E \in [-2.5\,\mathrm{eV}, 0]$ are distributed with $1 - f$ instead. Now, by putting $\beta = k_B T$ and $k = \frac{E}{v_F \hbar}$ we can write:

$$n_e = \frac{1}{2\pi}\left(\frac{1}{v_F\hbar}\right)^2 \int_0^{2.5\,\mathrm{eV}} f E\, dE = \frac{1}{2\pi}\left(\frac{1}{v_F\hbar}\right)^2 \int_0^{2.5\,\mathrm{eV}} \frac{E}{\exp\left(\beta(E - eV)\right) + 1} dE, \tag{A.8}$$

and similarly

$$n_h = \frac{1}{2\pi}\left(\frac{1}{v_F\hbar}\right)^2 \int\limits_{-2.5\,\mathrm{eV}}^{0} \frac{|E|}{\exp\big(\beta(eV-E)\big)+1}\,dE. \tag{A.9}$$

The final approximation comes from the specific regime that we work in. Since we are interested in $\beta V < \mathcal{O}(1)$ the temperature becomes the main energy scale. The range of temperatures is $\mathcal{O}\,(\mathrm{m\,eV})$ - meaning that charge carriers with energies bigger than 1 eV don't get excited. In particular for energies larger than 1 eV the integrand goes to zero exponentially. We can then write:

$$\begin{aligned} n_e &\approx \frac{1}{2\pi}\left(\frac{1}{v_F\hbar}\right)^2 \int\limits_{0}^{\infty} \frac{E}{\exp\big(\beta(E-eV)\big)+1}\,dE = \frac{1}{2\pi}\left(\frac{1}{\beta v_F\hbar}\right)^2 \int\limits_{0}^{\infty} \frac{x}{\exp\big(x-\beta eV\big)+1}\,dx, \\ &= \frac{-1}{2\pi}\left(\frac{k_B T}{v_F\hbar}\right)^2 \mathrm{Li}_2\left(-\exp(\beta eV)\right). \end{aligned} \tag{A.10}$$

The second step in this equation involves the substitution $x = \beta E$ and in the last step we use a well known result known as a complete Fermi - Dirac integral [24]. The Li_2 is the poly-logarithm function of order 2.

Similar derivation can be done for holes, resulting in:

$$\begin{aligned} n_h &\approx \frac{1}{2\pi}\left(\frac{1}{v_F\hbar}\right)^2 \int\limits_{-\infty}^{0} \frac{|E|}{\exp\big(\beta(eV-E)\big)+1}\,dE = \frac{1}{2\pi}\left(\frac{1}{\beta v_F\hbar}\right)^2 \int\limits_{-\infty}^{0} \frac{|x|}{\exp\big(\beta eV-x\big)+1}\,dx, \\ &= \frac{-1}{2\pi}\left(\frac{k_B T}{v_F\hbar}\right)^2 \mathrm{Li}_2\left(-\exp(-\beta eV)\right). \end{aligned} \tag{A.11}$$

Adding the two contributions together we see (including factors of 2 due to spin and valley degeneracy):

$$n_e + n_h = \frac{2_s 2_v}{4\pi}\left(\frac{k_B T}{v_F\hbar}\right)^2 \left(\left(\frac{eV}{k_B T}\right)^2 + \frac{\pi^2}{3}\right). \tag{A.12}$$

To get a feel for the numbers its useful to realize that since $\frac{eV}{k_B T} < \mathcal{O}(1)$ we can simplify even further and state $n_e + n_h \approx C_{tot} T^2$ with $C_{tot} = 1.43 \times 10^6\,\mathrm{cm^{-2}\,K^{-2}}$. Therefore, in the temperature range of $[100, 300]$ we shall see $\mathcal{O}\left(1\times 10^{10}\,\mathrm{cm^{-2}}\right)$ charge carriers.

Another important quantity is the charge imbalance. Here we compute:

$$n_h - n_e \approx \frac{2_s 2_v}{2\pi}\left(\frac{k_B T}{v_F\hbar}\right)^2 \left(\log(4)\frac{eV}{k_B T} + O\left(\frac{V^3}{T^3}\right)\right) \approx C_{imb} T V, \text{ with } C_{imb} \approx 1.45\times 10^{10}\,\mathrm{K^{-1}\,V^{-1}\,cm^{-2}}, \tag{A.13}$$

one can see that the charge polarization ρ_{pol} (ratio of charge imbalance and total charge) reads:

$$\rho_{pol} = \frac{C_{imb}}{C_{tot}}\frac{V}{T} \approx \frac{V}{T}\times 10^4. \tag{A.14}$$

Since temperature is $O(100)$ we must have the voltage being $O\left(10^{-3}\right)$ in order for the results to be lower than 1. If we restate this result in terms of energy, that is the ratio of (bias) potential and thermal energy we recover our regime defining statement $\rho_{pol} \approx \frac{\mathrm{eV}}{k_B T} < 1$.

Lastly lets compute the average (kinetic) energy, starting from the total energy. We will use the same substitution as before and the same approximations:

$$\begin{aligned} E_{tot} &\approx \frac{2_s 2_v}{2\pi}\left(\frac{1}{v_F\hbar}\right)^2 \left(\int\limits_{-\infty}^{0} \frac{|E|^2}{\exp\big(\beta(eV-E)\big)+1}\,dE + \int\limits_{0}^{\infty} \frac{E^2}{\exp\big(\beta(E-eV)\big)+1}\,dE\right) \\ &= \frac{2_s 2_v}{2\pi}\frac{(k_B T)^3}{(v_F\hbar)^2} \left(\int\limits_{-\infty}^{0} \frac{x^2}{\exp\big(\beta eV-x\big)+1}\,dx + \int\limits_{0}^{\infty} \frac{x^2}{\exp\big(x-\beta eV\big)+1}\,dx\right) \\ &= \frac{2_s 2_v}{2\pi}\frac{(k_B T)^3}{(v_F\hbar)^2} \left(-2\,\mathrm{Li}_3(-\exp(-\beta eV)) - 2\,\mathrm{Li}_3(-\exp(\beta eV)))\right) \\ &\approx \frac{2_s 2_v}{2\pi}\frac{(k_B T)^3}{(v_F\hbar)^2} \left(3\zeta(3) + 2\log(2)\left(\frac{eV}{k_B T}\right)^2 + O\left(\frac{V^4}{T^4}\right)\right). \end{aligned} \tag{A.15}$$

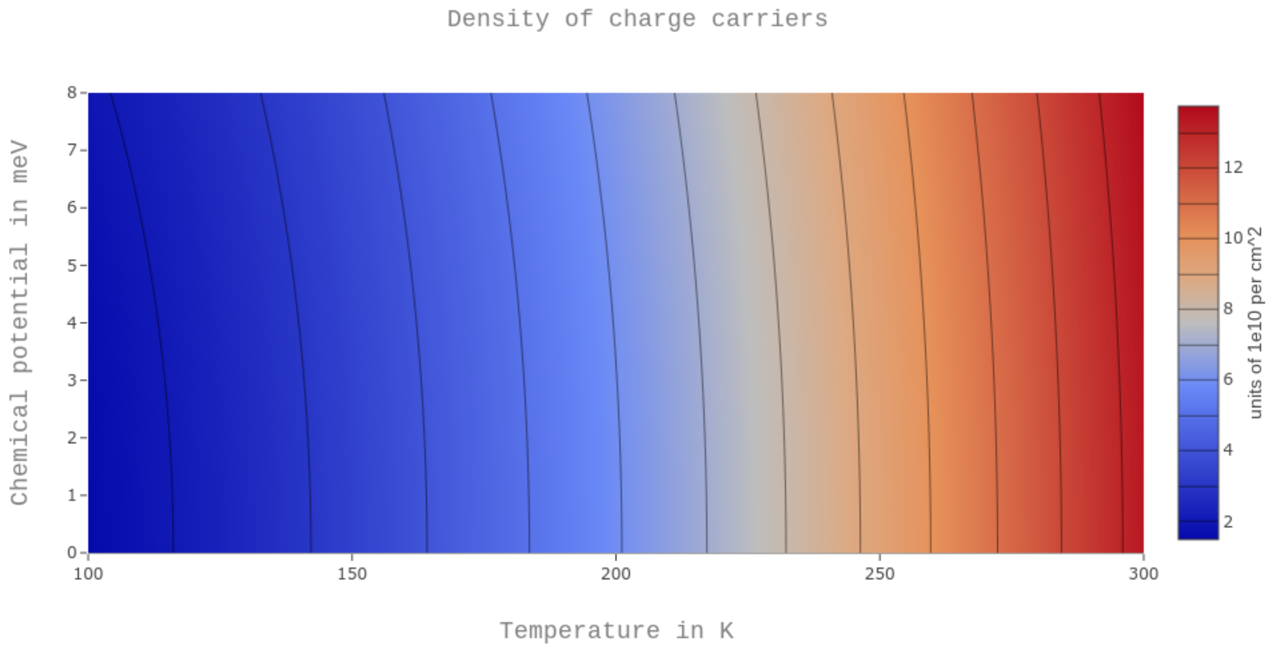

Figure A.2: The density of the charge carriers per square cm. The case of $\mu < k_B T$ is shown such that typical densities are of the order $1 \times 10^{10}\,\mathrm{cm}^{-2}$. Typical values in the case of $\mu > k_B T$ are $1 \times 10^{12}\,\mathrm{cm}^{-2}$ hoewever this region is not regarded within this context.

In the last line the Riemann Zeta function ζ [24] makes an appearance. From here we compute the average kinetic energy as:

$$
\begin{aligned}
< E > = E_{tot}/(n_e + n_h) &= 2k_B T \left(\frac{9\zeta(3) + 6\log(2)x^2}{\pi^2 + 3x^2} \right), \\
&\approx 2.2 k_B T + 0.1 \frac{(eV)^2}{k_B T} + O\left(\frac{V^4}{T^3} \right).
\end{aligned}
\tag{A.16}
$$

This might be a somewhat puzzling result. One would expect a typical $\frac{1}{2} k_B T$ per degree of freedom, in accordance with the equipartition theorem. This is not the case for Graphene because the kinetic energy term is linear in momentum.

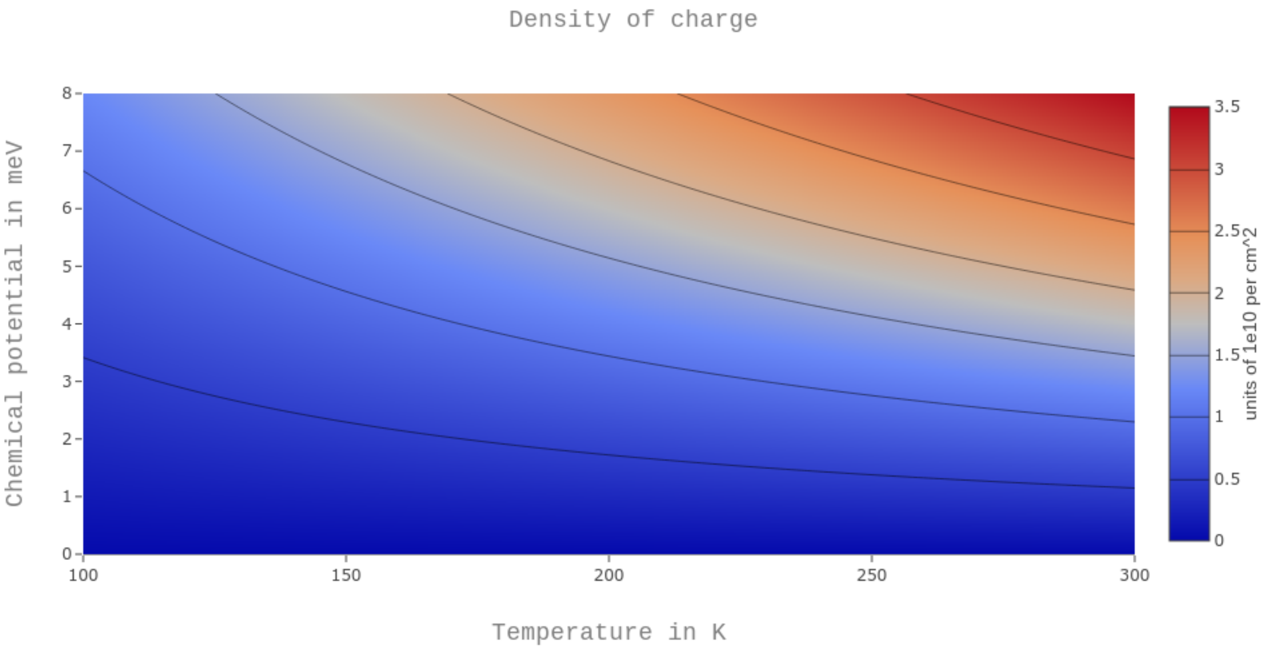

Figure A.3: The density of the charge per square cm. At higher chemical potentials this value coincides exactly with the charge carrier density. However at low μ the netto charge is low because we have two types of charge carriers. This quantity is of imporantance when considering the type of interaction - at low imbalance most of the interactions will be attractive and as we go up we shall see more repulsive ones.

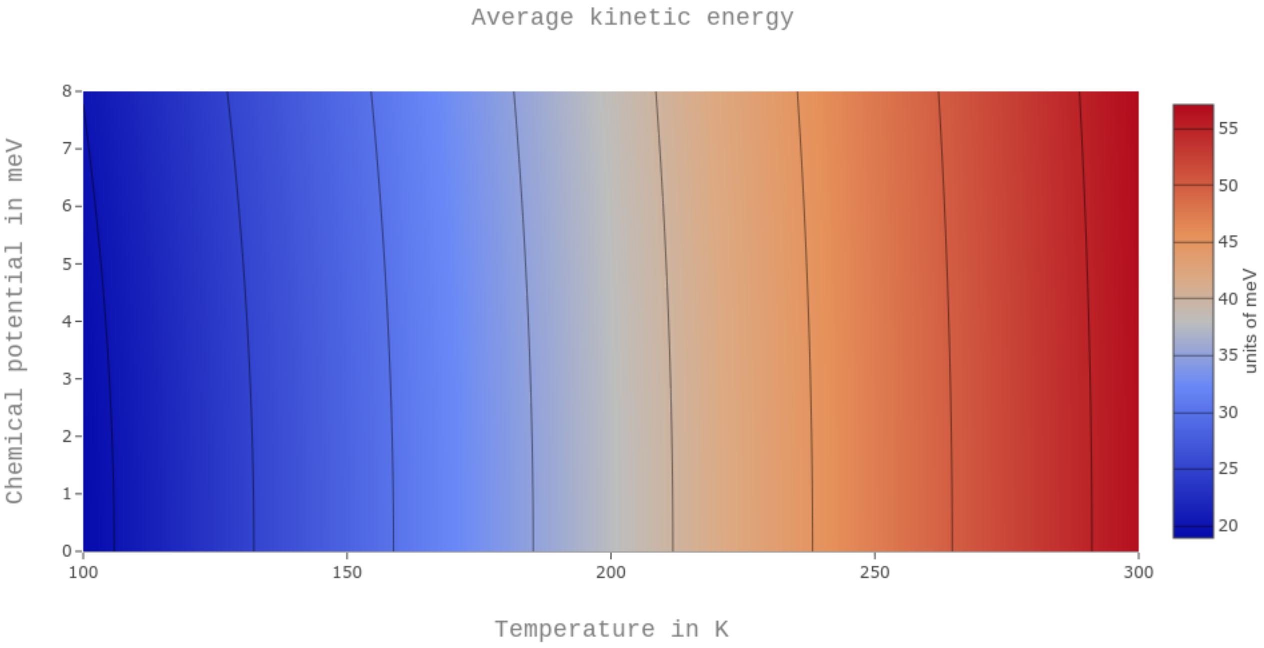

Figure A.4: The average kinetic energy as function of T and μ. While the T dependency is roughly linear we do see slight additional μ effects. When $\mu > k_B T$ this relation will change - the dependency will be mostly quadratic in μ with slight temperature dependence.

B

Leapfrog properties and stability

> Isn't that ingenious? I borrowed it straight from Newton. It comes right out of the Principia, diagram and all.
>
> *R. Feynman 1965*

B.1. Mathematical background of the numerical integration scheme

This section will be based on [4] and [12]. Author would like to thank users of mathstackexchange for contributing to understanding of these topics.
Consider a function f of parameters r and p. Then we can express the time derivative as:

$$\frac{d}{dt} f\left(p(t), r(t)\right) = \left(\dot{p}\frac{\partial}{\partial p} + \dot{r}\frac{\partial}{\partial r}\right) f\left(p(t), r(t)\right). \tag{B.1}$$

If we now introduce the momentum and position shift operators - operators moving the coordinates forward in time as $iL_p t = \dot{p}\frac{\partial}{\partial p} t$ and $iL_r = \dot{r}\frac{\partial}{\partial r} t$ respectively, then it's clear to see that the proper solution of B.1 reads:

$$f\left(p(t), r(t)\right) = \exp\left(it\left(L_p + L_R\right)\right) f\left(p(0), r(0)\right).$$

Note that this has not solved the equation in any way or shape. We simply restated the problem of finding a solution to a PDE into one of determining the action of an exponential operator. In particular, since L_p and L_r don't commute we can not split this exponential into separate ones. Luckily, in the 1950's Trotter [1] introduced a handy identity:

$$e^{A+B} = \lim_{N\to\infty}\left(e^{A/2N}e^{B/N}e^{A/2N}\right)^N. \tag{B.2}$$

More relevantl, for any finite N we have $e^{A+B} = \left(e^{A/2N}e^{B/N}e^{A/2N}\right)^N e^{O(N^{-2})}$. Now set $A = itL_p$, $B = itL_r$ and $t = N\Delta t$ we recover:

$$\exp\left(iL_p t + iL_r t\right) \approx \left(\exp\left(iL_p\Delta t/2\right)\exp(iL_r\Delta t)\exp\left(iL_p\Delta t/2)\right)\right)^N. \tag{B.3}$$

This last expression should be familiar, it is exactly the alternating pattern of updating momentum and position from Equation (3.2). The sympletic property, conservation of Hamiltonian, can be now understood. The error term reads $\exp O(\Delta t^2) \approx \mathbb{1}$. Simpler methods like the Euler-Forward method (based on the Baker–Campbell–Hausdorff formula [12] $\exp(A+B) = \lim_{N\to\infty}\left(\exp A/N \exp B/N\right)^N$) do not have such nice error properties and will thus drift in energy on long timescales.

B.2. Error terms

One should realize that Equation (B.2) only holds for bounded operators A and B. In case they are not bounded, we get something called breakdown of stability. This causes the energy, and in our case momentum, to suddenly grow to a huge number. According to [13] it is extremely hard to find any bound on Δt that will ensure the stability of the algorithm in the case of unbounded Hamiltonian analytically. We will, however, try to give some intuition as to what goes wrong and why graphene tends to break stability while typically for $H = p^2 + 1/r$ the simulations remain stable. The one timestep approximation can be written as:

$$\exp\big(iL_p\Delta t/2\big)\exp(iL_r\Delta t)\exp\big(iL_p\Delta t/2\big) = \exp\big(iL_r\Delta t + iL_p\Delta t + \epsilon\big), \tag{B.4}$$

with ϵ a term containing all odd numbered (starting from 3) commutators of $iL_r\Delta t$ and $iL_p\Delta t$. That is we do not conserve the Hamiltonian. Rather, we conserve a quantity that tends to be near our Hamiltonian since all the terms in ϵ are at least $O(\Delta t^3)$. However, we will show that when particles get close to each other this quantity needs not to be small. It may in fact dominate the operator. Using a approach similar to [13] and working on separable Hamiltonian $H = K(p) + V(r)$ we can write the leading term of ϵ out as:

$$\epsilon \approx (\Delta t)^3\left(\frac{1}{24}\left[iL_r,\left[iL_r,iL_p\right]\right] + \frac{1}{12}\left[iL_p,\left[iL_r,iL_p\right]\right]\right) \approx (\Delta t)^3\left(\frac{1}{24}V_r^2K_{pp} + \frac{1}{12}V_{rr}K_p^2\right). \tag{B.5}$$

Lets now give crude approximations of the product of derivatives V_r, V_{rr}, K_p and K_{pp} in terms of powers of p and r. Remember, we consider the case of two particles being attracted towards each other therefore $p \sim \frac{1}{r}$ for graphene and $p^2 \sim \frac{1}{r}$ for 2DEG. For graphene we have:

$$\epsilon \sim \Delta t^3\left(\frac{1}{r^3}\right) \sim \frac{\Delta t^3}{r^3} \tag{B.6}$$

while for 2DEG we obtain:

$$\epsilon \sim \Delta t^3\left(\frac{1}{r^4} + \frac{p^2}{r^3}\right) \sim \frac{\Delta t^3}{r^4}. \tag{B.7}$$

Therefore, for ϵ to be small we need $\Delta t \ll r$ for graphene while 2DEG only requires $\Delta t \ll r^{4/3}$ - a constraint trivially fulfilled by requiring the particles to move less than half of the distance in between particles. The case for graphene is harder, it is not clear what the relevant prefactor needs to be. Furthermore, looking at higher order terms of ϵ complicates things even further.

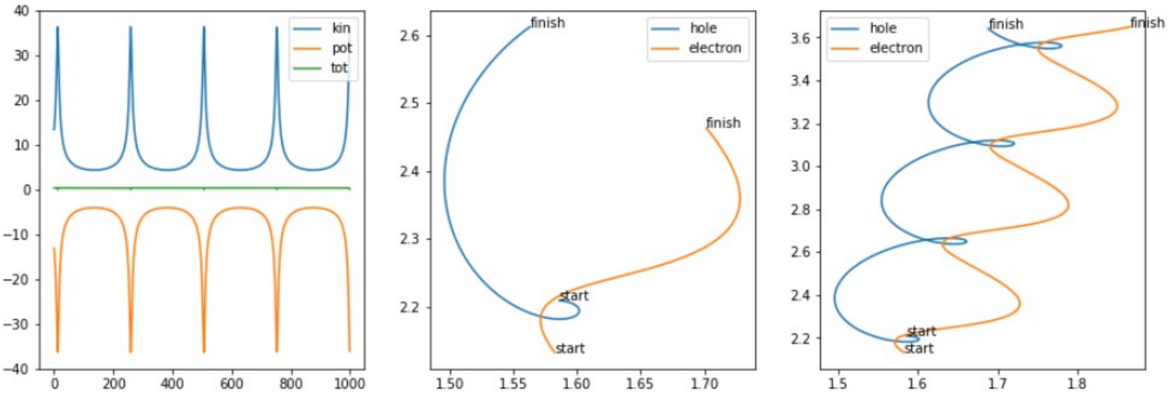

Figure B.1: E-H interactions in a classical system (kinetic energy quadratic in momentum). The left panel shows energy (in a.u.) conservation. The middle and right panels show the time-evolution of the system. One can correlate the high potential energy to proximity between particles, we see full stability of the integration method as perdicted by Eq (B.7).

B.3. Bouncing

We write the momentum of the pair in the basis of vector between the particles $\mathbf{r}_{ij}$ and a vector orthogonal to it $\mathbf{r}_\perp$. So we write:

$$p_i = \begin{pmatrix} a \\ b \end{pmatrix}, \quad p_j = \begin{pmatrix} c \\ d \end{pmatrix}. \tag{B.8}$$

The velocity still equals the direction of momentum so if $\frac{a}{|p_i|} - \frac{c}{|p_j|} < 0$ the particles are moving towards each other. Our goal is to find a transformation such that the new velocities point away from each other. Conservation of momentum tell us that if p_i is changed by $[x, y]$ then the opposite must be done for p_j. Furthermore, if

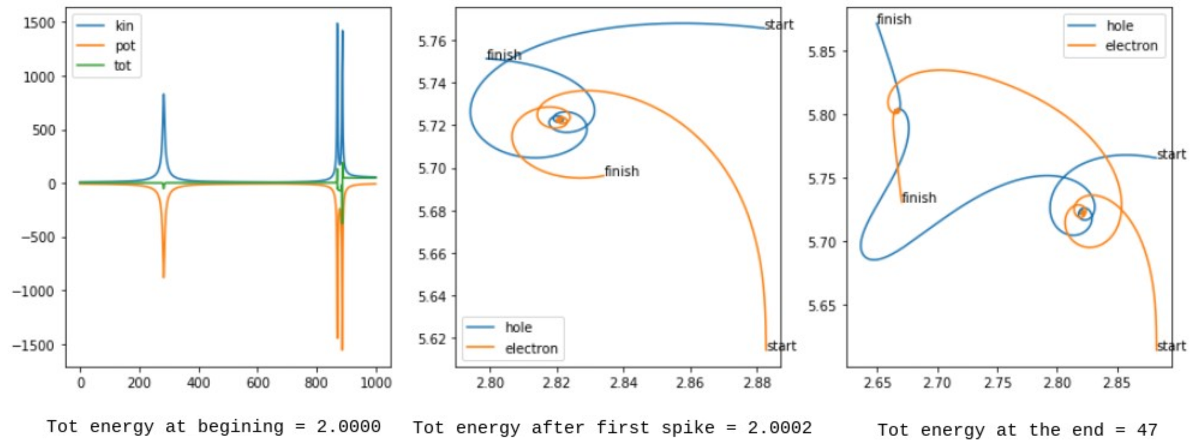

Figure B.2: E-H interactions in a graphene, kinetic energy linear in momentum without the bouncing mechanism. The left panel shows energy (in a.u.) as a function of time. Two collision events are visible. The first one is conserving energy and second one is not. Middle and right panels the show time-evolution of the system. The curvature of paths leaving in the right (non-conserving) collision show the stability break down - the particles gained extra momentum due to Eq (B.6).

we choose the origin to be exactly between the two particles, the conservation of angular momentum allows only for changes to be made in the direction of $\mathbf{r}_{ij}$ and thus $y = 0$.

All that is left is the conservation of (kinetic) energy. We write:

$$\sqrt{a^2+b^2}+\sqrt{c^2+d^2}=\sqrt{(a-x)^2+b^2}+\sqrt{(c+x)^2+d^2}. \tag{B.9}$$

The equation is trivially solved by $x = 0$ but there exists a more impressive solution:

$$\begin{aligned} x &= \frac{A}{B} \text{ with} \\ A &= 2(2a^3d^2 - b^2c|p_i||p_j| - ab^2|p_i||p_j| + \\ &\quad cd^2|p_i||p_j| + ad^2|p_i||p_j| + a^2b^2c + \\ &\quad a^2cd^2 - ab^2c^2 + ab^2d^2 - ac^2d^2 - ad^4 + \\ &\quad b^4c - 2b^2c^3 - b^2cd^2) \\ B &= 4a^2d^2 + 4ab^2c + 4acd^2 - b^4 + 4b^2c^2 + 2b^2d^2 - d^4. \end{aligned}$$

We postulate (without proving it) that this transformation does indeed flip the velocities away from each other.

C

Smoothing of local observables

C.1. Physical observables as functions of spatial coordinates

In the semiclassical approach, we consider point-particles. The "point" part of the name refers to the idea of the particles being located in one specific point in phase space. Therefore, classically when we discuss the quantity of "density" we usually define some test volume V_{test} and compute:

$$\rho = \frac{1}{V_{\text{test}}} \iint\limits_{V_{\text{test}}} \text{DoS}(\mathbf{x}) d\mathbf{x} \quad \text{with} \quad \text{DoS}(\mathbf{x}) := \sum_{p \in \text{Particles}} \delta(\mathbf{x} - \mathbf{x_p}). \tag{C.1}$$

Such defined density ρ works very well in big systems. In particular, if there are many particles and they are somewhat uniformly spread out, the density will not change rapidly if we change the test volume, making the quantity well defined.

Local density is definitely a quantity of interest for my system. Yet, the scale of the problem makes finding right V_{test} difficult. Consider a toy model: a system with only one particle. Subdividing such a system into a grid of test volumes would give a local density of zeros almost everywhere and $\rho = \frac{1}{V_{\text{test}}}$ in one of the grid points. This would result in a serious discontinuity in the local density function at the border of the test volume with the particle in it and its neighbours. Furthermore, as we look at behavior in the limit $V_{test} \to 0$ the jump would only get worse!

One might argue that the problems aren't relevant because the concept of "density" is rather meaningless for such a system. To this I would like to propose another layer to the toy model. Lets now say that this one particle is a random walker and that we record the local density for each time, denoted by $\rho(x,t)$. Since this particle will now travel the system randomly we expect

$$\lim_{T\to\infty} \frac{1}{T} \int\limits_0^T \rho(x,t) dt = \frac{1}{A}$$

with A being the total area of the system. That is, the *time* average simply states "there are no areas with more density than others". Similar ideas can be introduced when considering *ensemble* averages. Ensemble averaging is the process of taking the average over all possible configurations of a system. Surely if we average over all possible positions of our particle, we would obtain the exact same result as time averaging. Within the framework of this project we shall exchange ensemble averaging by time averaging due to ergodicity of the system.

In the example of a one-time step and one particle we see a huge variance between grid spaces. Let us quantify this by making the random walker jump between grid points, each with chance $p = \frac{V_{\text{test}}}{A}$. Particle being on specific grid i is then a Bernoulli variable with parameter p. The expected value of the local density on grid point i would be $\mathbb{E}(\rho_i) = p\frac{1}{V_{\text{test}}} + (1-p)\cdot 0 = \frac{1}{A}$, as shown before. The variance will read

$$\sigma^2(\rho_i) = p\left(\frac{1}{V_{test}}\right)^2 - \left(\frac{1}{A}\right)^2 = \frac{1}{A}\left(\frac{A - V_{test}}{AV_{test}}\right) \approx \frac{1}{A}\frac{1}{V_{test}} \tag{C.2}$$

where in the last line we use $A \gg V_{\text{test}}$. Since σ^2 goes down as t^{-1} with t the number of samples, we would need to wait until $tV_{\text{test}} \gg 1$ for variance to decrease. In the framework of this project the situation is even more dire because particles are not random walkers but correlated movers, they take a finite amount of time to move between grid sides.

Wince we know that the outcome equals $\frac{1}{A}$ we can define a new, smoothed out DoS in such that the convergence rate of the density is speed up. The optimal shape of this smoothed out DoS is a difficult question but it isn't of actual relevance to us, since the physical phenomena arising from the exact shape of the wave function will not be visible within this model anyway. We can simply propose a reasonable shape of a Gaussian peak, as it reassembles a Dirac peak (in the limit $\sigma \to 0$). This changes the DoS:

$$\sum_{p\in\text{Particles}} \delta(\mathbf{x}-\mathbf{x_p}) \to \sum_{p\in\text{Particles}} \frac{1}{\sqrt{2\pi\sigma^2}} \exp\left(-\frac{(\mathbf{x}-\mathbf{x_p})^2}{2\sigma^2}\right) \tag{C.3}$$

We can now reevaluate equation C.1.

$$\begin{aligned}\rho_i &= \frac{1}{V}\iint\limits_{V_{test}} \text{DoS}(\mathbf{x})\,d\mathbf{x} = \frac{1}{\sqrt{2\pi\sigma^2}V}\sum_{p\in\text{Particles}}\left(\int \exp\left(-\frac{(x-x_p)^2}{2\sigma^2}\right)dx\right)\left(\int \exp\left(-\frac{(y-y_p)^2}{2\sigma^2}\right)dy\right)\\ &= \frac{\sqrt{\pi\sigma^2}}{2\sqrt{2}V}\sum_{p\in\text{Particles}}\left[\text{erf}\left(\frac{x_p-x}{\sqrt{2\sigma^2}}\right)\right]\left[\text{erf}\left(\frac{y_p-y}{\sqrt{2\sigma^2}}\right)\right]\end{aligned} \tag{C.4}$$

where the evaluation of the integral is over the test volume. The only free parameter left in this expression is σ. A physically good choice is a fraction of typical particle-particle distance l_{pp}.

Using the local density we can now compute any local quantity A on grid point i as :

$$\begin{aligned}A_i &:= \frac{\sqrt{\pi\sigma^2}}{2\sqrt{2}V}\sum_{p\in\text{Particles}} A_p\left[\text{erf}\left(\frac{x_p-x}{\sqrt{2\sigma^2}}\right)\right]\left[\text{erf}\left(\frac{y_p-y}{\sqrt{2\sigma^2}}\right)\right]\\ \text{with}\quad & A_{i,\text{per particle}} := A_i/\rho_i.\end{aligned} \tag{C.5}$$

Bibliography

[1] AMS :: Proceedings of the American Mathematical Society, . URL `http://www.ams.org/journals/proc/1959-010-04/S0002-9939-1959-0108732-6/home.html`.

[2] Introduction to Electrodynamics, 4th Edition, . URL `https://www.pearson.com/us/higher-education/program/Griffiths-Introduction-to-Electrodynamics-4th-Edition/PGM249908.html`.

[3] Minimum of Resistance in Impurity-free Conductors r.N. Gurzhi, . URL `http://www.jetp.ac.ru/cgi-bin/e/index/e/17/2/p521?a=list`.

[4] *Understanding Molecular Simulation.* Elsevier, 2002. ISBN 9780122673511. doi: 10.1016/B978-0-12-267351-1.X5000-7. URL `https://linkinghub.elsevier.com/retrieve/pii/B9780122673511X50007`.

[5] D. A. Bandurin, I. Torre, R. Krishna Kumar, M. Ben Shalom, A. Tomadin, A. Principi, G. H. Auton, E. Khestanova, K. S. Novoselov, I. V. Grigorieva, L. A. Ponomarenko, A. K. Geim, and M. Polini. Negative local resistance caused by viscous electron backflow in graphene. *Science*, 351(6277):1055–1058, March 2016. ISSN 0036-8075, 1095-9203. doi: 10.1126/science.aad0201. URL `http://arxiv.org/abs/1509.04165`. arXiv: 1509.04165.

[6] Luca Banszerus, Michael Schmitz, Stephan Engels, Matthias Goldsche, Kenji Watanabe, Takashi Taniguchi, Bernd Beschoten, and Christoph Stampfer. Ballistic Transport Exceeding 28 μm in CVD Grown Graphene. *Nano Letters*, 16(2):1387–1391, February 2016. ISSN 1530-6984. doi: 10.1021/acs.nanolett.5b04840. URL `https://doi.org/10.1021/acs.nanolett.5b04840`.

[7] U. Briskot, M. Schütt, I. V. Gornyi, M. Titov, B. N. Narozhny, and A. D. Mirlin. Collision-dominated nonlinear hydrodynamics in graphene. *Physical Review B*, 92(11), September 2015. ISSN 1098-0121, 1550-235X. doi: 10.1103/PhysRevB.92.115426. URL `http://arxiv.org/abs/1507.08946`. arXiv: 1507.08946.

[8] Mani Chandra, Ravishankar Sundaraman, and Deshdeep Sahdev. AC $>$ DC: Vortex Generation, Reconnection and Temporal Correlations in Electronic Hydrodynamics. *arXiv:1803.10037 [cond-mat, physics:physics]*, March 2018. URL `http://arxiv.org/abs/1803.10037`. arXiv: 1803.10037.

[9] S. Das Sarma, Shaffique Adam, E. H. Hwang, and Enrico Rossi. Electronic transport in two-dimensional graphene. *Reviews of Modern Physics*, 83(2):407–470, May 2011. doi: 10.1103/RevModPhys.83.407. URL `https://link.aps.org/doi/10.1103/RevModPhys.83.407`.

[10] Gregory Falkovich and Leonid Levitov. Linking Spatial Distributions of Potential and Current in Viscous Electronics. *Physical Review Letters*, 119(6), August 2017. ISSN 0031-9007, 1079-7114. doi: 10.1103/PhysRevLett.119.066601. URL `http://arxiv.org/abs/1607.00986`. arXiv: 1607.00986.

[11] Haoyu Guo, Ekin Ilseven, Gregory Falkovich, and Leonid Levitov. Higher-Than-Ballistic Conduction of Viscous Electron Flows. *Proceedings of the National Academy of Sciences*, 114(12):3068–3073, March 2017. ISSN 0027-8424, 1091-6490. doi: 10.1073/pnas.1612181114. URL `http://arxiv.org/abs/1607.07269`. arXiv: 1607.07269.

[12] Ernst Hairer, Syvert P. Nørsett, and Gerhard Wanner. *Solving Ordinary Differential Equations I: Nonstiff Problems.* Springer Series in Computational Mathematics, Springer Ser.Comp.Mathem. Hairer,E.:Solving Ordinary Diff. Springer-Verlag, Berlin Heidelberg, 2 edition, 1993. ISBN 9783540566700. URL `https://www.springer.com/gp/book/9783540566700`.

[13] Ernst Hairer, Christian Lubich, and Gerhard Wanner. *Geometric Numerical Integration: Structure-Preserving Algorithms for Ordinary Differential Equations.* Springer Series in Computational Mathematics. Springer-Verlag, Berlin Heidelberg, 2 edition, 2006. ISBN 9783540306634. URL `https://www.springer.com/gp/book/9783540306634`.

[14] E. H. Hwang and S. Das Sarma. Dielectric function, screening, and plasmons in 2d graphene. *Physical Review B*, 75(20), May 2007. ISSN 1098-0121, 1550-235X. doi: 10.1103/PhysRevB.75.205418. URL `http://arxiv.org/abs/cond-mat/0610561`. arXiv: cond-mat/0610561.

[15] E. M. Kirova and G. E. Norman. Viscosity calculations at molecular dynamics simulations. *Journal of Physics: Conference Series*, 653:012106, November 2015. ISSN 1742-6596. doi: 10.1088/1742-6596/653/1/012106. URL `https://doi.org/10.1088%2F1742-6596%2F653%2F1%2F012106`.

[16] Egor I. Kiselev and Joerg Schmalian. The boundary conditions of viscous electron flow. *arXiv:1806.03933 [cond-mat]*, June 2018. URL `http://arxiv.org/abs/1806.03933`. arXiv: 1806.03933.

[17] Valeri N. Kotov, Bruno Uchoa, Vitor M. Pereira, F. Guinea, and A. H. Castro Neto. Electron-Electron Interactions in Graphene: Current Status and Perspectives. *Reviews of Modern Physics*, 84(3):1067–1125, July 2012. doi: 10.1103/RevModPhys.84.1067. URL `https://link.aps.org/doi/10.1103/RevModPhys.84.1067`.

[18] R. Krishna Kumar, D. A. Bandurin, F. M. D. Pellegrino, Y. Cao, A. Principi, H. Guo, G. H. Auton, M. Ben Shalom, L. A. Ponomarenko, G. Falkovich, K. Watanabe, T. Taniguchi, I. V. Grigorieva, L. S. Levitov, M. Polini, and A. K. Geim. Superballistic flow of viscous electron fluid through graphene constrictions. *Nature Physics*, 13(12):1182–1185, December 2017. ISSN 1745-2473, 1745-2481. doi: 10.1038/nphys4240. URL `http://arxiv.org/abs/1703.06672`. arXiv: 1703.06672.

[19] Andrew Lucas and Kin Chung Fong. Hydrodynamics of electrons in graphene. *Journal of Physics: Condensed Matter*, 30(5):053001, February 2018. ISSN 0953-8984, 1361-648X. doi: 10.1088/1361-648X/aaa274. URL `http://arxiv.org/abs/1710.08425`. arXiv: 1710.08425.

[20] Subir Sachdev. The landscape of the Hubbard model. *String Theory and Its Applications*, pages 559–620, November 2011. doi: 10.1142/9789814350525_0009. URL `http://arxiv.org/abs/1012.0299`. arXiv: 1012.0299.

[21] Chaitanya K. Ullal, Jian Shi, and Ravishankar Sundararaman. Electron mobility in graphene without invoking the Dirac equation. *arXiv:1806.10027 [cond-mat]*, June 2018. URL `http://arxiv.org/abs/1806.10027`. arXiv: 1806.10027.

[22] F. T. Vasko and V. V. Mitin. Generation-recombination processes via acoustic phonons in a disorded graphene. *Physical Review B*, 84(15), October 2011. ISSN 1098-0121, 1550-235X. doi: 10.1103/PhysRevB.84.155445. URL `http://arxiv.org/abs/1107.2708`. arXiv: 1107.2708.

[23] Wang Yao, Shengyuan A. Yang, and Qian Niu. Edge States in Graphene: From Gapped Flat-Band to Gapless Chiral Modes. *Physical Review Letters*, 102(9):096801, March 2009. doi: 10.1103/PhysRevLett.102.096801. URL `https://link.aps.org/doi/10.1103/PhysRevLett.102.096801`.

[24] Daniel Zwillinger. *Table of Integrals, Series, and Products.* Elsevier, September 2014. ISBN 9780123849342. Google-Books-ID: NjnLAwAAQBAJ.